Fabrication and characterisation of high aspect ratio MEMS electrochemical sensor
Dongbin Cai

TUDelft

Fabrication and characterisation of high aspect ratio MEMS electrochemical sensor

by

Dongbin Cai

to obtain the degree of Master of Science
at the Delft University of Technology,
to be defended publicly on Tuesday November 28, 2017 at 10:00 AM.

Student number: 4379640
Thesis committee: Prof. Dr Kouchi. Zhang,   Professor ECTM, TU Delft,
                    Dr. Jia. Wei,   EKL, TU Delft, Daily supervisor
                    Dr. Andre . Bossche,   Assistant Professor, TU Delft
                    Ir. Manjunath R. Venkatesh, TU Delft, Daily supervisor

T̃U Delft

Science is a wonderful thing
if one does not have to earn one's living at it.

Albert Einstein

Contents

Preface

A high aspect ratio and large current 3D electrochemical sensor was designed. This miniaturized sensor was built by using silicon microfabrication technologies in comparison to screen printed electrode. New tilting tool for CHA solution platinum evaporator is designed and realized. The analysis of tilt angles and rotation for evaporation of platinum on 3D structure in evaporator is done. Different recipe of DRIE etching have been tested in order to get straight pillars. Different recipe in both "Trikon Omega 201" and "Rapier Omega i2L DRIE etcher" were tested to minimise the scalloping effects on the pillars. The final sensor with straight pillar structure with platinum working electrode is fabricated.

Keywords: Electrochemical sensor; Voltammetric sensing; Silicon sensor; Platinum electrode

Dongbin Cai Delft, 28 November 2017

1

Introduction

1.1. Electrochemical Sensor

In the field of electrochemistry and analytical chemistry, electrochemical sensor plays an important role and becoming popular. This technique can transfer complicate chemical phenomena to electrical signal such as electron transfer and charge separation. A natural development of the understanding of electrochemical processes, their kinetics and mechanism is to use this knowledge to identify and quantify species present either by themselves in "inert" media or selectively in complex matrices. Identification comes through measurement of the potential at which the electrode reaction occurs. Quantification comes through measurements of current, charge or potential. Three types of electro analytical measurement can be distinguished which can all be employed in electrochemical sensing: conductimetric, potentiometric ,voltammetric and amperometric, and which will be discussed further below in the next section. Of these, conductimetric is the least versatile as it offers no species selectivity but the principles of operation are relatively simple; nevertheless, it can be important in certain applications. Well-controlled experimental conditions are needed with sufficiently good or sophisticated experimental devices and instrumentation. This can represent a significant challenge when applying sensors in the areas of health, food and the environment.

In a situation where identification and quantitative data of an analysis are needed, a number of questions arise with regard to selectivity, sensitivity and detection limit, besides an assessment of the uncertainties. For the chemist who wishes to develop electrochemical sensors, a good knowledge of the fundamentals of electrochemistry, i.e. an understanding of the processes that can occur in terms of transport of species in solution, the thermodynamics and kinetics of electron transfer and the influence of the surface, particularly the inter facial region, is crucial. Other areas of chemistry are also very important to delineating and putting into practice any

1

good sensing strategy and which must combine these criteria with the requirements of accuracy, sufficiently low uncertainty, good reproducibility and repeatability as well as functionality and practicality.

1.2. Types of electrochemical sensing principles

Electrochemical sensing can be divided into three areas:

Conductimetric

Conductimetric Measurement of solution resistance enables the deduction of the concentration of charge between two electrodes. Such measurements are not species selective, but are used coupled in conjunction with separation techniques such as high performance liquid chromatography.[1]

Potentiometric

Potentiometric The equilibrium potential of an indicator electrode is measured against a selected reference electrode at zero current using a potentiometer (approximated to by using a high-impedance voltmeter). Ion-selective electrodes, if a suitable electrode material can be found, can give good selectivity to one particular species, in many cases with only minimal interference from other ions. Measurement of non-equilibrium potentials is also used in potentiometric analysis, but less frequently.[1]

Voltammetric

A current–voltage profile is recorded where the current is registered as a function of applied potential using a potentiostat (or potential is recorded as a function of applied current using a galvanostat). Usually three electrodes are necessary—working (indicator), auxiliary and reference electrodes; the reference electrode can also serve as auxiliary electrode if the currents are very small. More information and lower detection limits can be achieved than with potentiometric sensors, and more than one electroactive species, if each reacts at different applied potentials, can be determined in the same experiment. Thus, in the most easily applicable situations for these types of sensor, there is no need for prior separation of components of complex mixtures.[1]

Amperometric

Amperometric biosensors works by the creating of a current when a voltage is applied between two electrodes. This kind of sensors generally have dynamic ranges, response times and sensitivities similar to the potentiometric biosensors. [1]

1.3. Voltammetric sensors

The first voltammetric system which was able to examine current–voltage profiles in a useful way from a sensing point of view, was the dropping mercury electrode (DME) invented by Heyrovsky in 1922, and for which he won

the Nobel prize in 1959—designated polarography Unlike potentiometric sensors[2], dynamic processes are probed. This could be used for the measurement of reducible species in solution (but unfortunately for only a few oxidisable ones owing to the oxidation of mercury itself). The first reproducible measurements of many species were carried out through selective reduction based on their half-wave potentials, particularly metal ions, as well as to studies of the mechanism of reduction and quantification of many organic species. An extremely important advantage of liquid mercury is its very wide negative potential range in aqueous solutions due to a high overpotential for the evolution of hydrogen, unmatched by any other electrode material. The cyclic operation of the dropping mercury electrode has continuous drop growth at the end of a tiny capillary until it falls due to gravity and another begins to form. It is therefore a hydrodynamic electrode in the sense that there is imposed convection, caused by movement (growth) of the electrode (drop) itself, rather than movement of the solution. Thus, if the experimental data are treated in the correct way, pseudo-steady-state voltammograms can be constructed. The DME was a breakthrough and continued to be exploited for many years but further practical developments were slow because the associated control and analysis instrumentation was not sufficiently sophisticated. This changed when integrated circuits appeared that enabled current sampling, in a simple way, at particular points of drop growth. It led to widespread implementation of normal and differential pulse polarography, where pulses were synchronised with the drops so as to be applied close to the end of drop life. Once this was achieved, other waveforms could follow, such as square wave polarography[3]; this had already been proposed at the beginning of the 1950s, but had not been properly implemented due to insufficiently good electronics. The hanging mercury drop electrode, now largely replaced by the static mercury drop electrode, removed the periodic variation in current owing to drop growth which was also one of the main advantages, especially with organic compounds, of avoiding long-term adsorption on the mercury surface. There was clearly a need to use other electrode materials which enable sensing in the positive potential range by oxidation and preferably give access to both positive and negative potential ranges. The first materials to be examined for this purpose were the noble metals, platinum and gold, and silver to a lesser extent. This allowed making solid electrodes of different shapes and sizes but did not solve the question of reproducibility, unless very efficient and constant stirring could be carried out. Electrode materials based on different forms of carbon were developed, sometimes with inferior electrode kinetics but with the advantage of being more economically accessible than the noble metals. Other materials have followed. One of the more interesting is bismuth which has a wide negative potential range that is nearly as good as mercury, without toxicity problems. Procedures for solid electrode surface cleaning and conditioning have been devised which aid in diminishing some of the difficulties associated with contamination of solid surfaces.

1

This question of the obtaining of steady-state, reproducible data at solid electrodes was solved with forced convection, either of the electrodes themselves or of the solution. The best example of the former is rotating disc and ring-disc electrodes and of the latter channel/tube or wall jet [4]. True steady-state current–voltage

profiles can be recorded in these cases. The diffusion limited current is directly proportional to concentration (the potential can be fixed at this value and the current recorded as a function of concentration), and the shape of the voltammetric curve may give some kinetic information. However, even with high convection rates, the detection limit is of the order of 10^{-4} M. This can be significantly improved by the use of pre-concentration techniques such as stripping voltammetry, the different timescales of the preconcentration and determination steps enabling lower concentrations to be measured. Pulse techniques, particularly differential pulse voltammetry and square wave voltammetry, have flourished in terms of their breadth of application since the 1970s at solid electrodes and are particularly easy to implement with digital-based instrumentation. Due to their transient nature, these allow a reduction in detection limit by a factor of 1,000. They also allow the probing of the electrode kinetics at the same time as they are giving analytical information. Square wave voltammetry has the added advantage that it is fast so that, besides reducing experimental time, problems associated with dissolved oxygen are less, very valuable with pre-concentration stripping voltammetric procedures which can reach down to 10^{-9} M or even lower. Alternating current voltammetry began to show much promise in the 1960s and 1970s before the advent of instruments which enable the use of pulse techniques. Cyclic and linear sweep voltammetry had shown themselves not able to go much below 10^{-5} M. Although the information which is obtained by ac voltammetry is equivalent in terms of sensitivity and detection limit to pulse voltammetry, owing to the digital nature of modern electrochemical instruments, it is not much used. However, electrochemical impedance spectroscopy using small alternating voltage perturbations has increased in scope with applications in sensor characterisation becoming more common and impedimetric sensing has been developed.

1.4. Advantages of electrochemical sensor

Consideration of the general characteristics of electrochemical sensors and these criteria allows the advantages of electrochemical sensing to be put forward. Most of these concern voltammetric/amperometric sensing: – The choice of electrode material can lead to selectivity in potentiometric and in voltammetric sensors. In potentiometric sensing, ion-selective electrodes are designed to be specific. In voltammetric sensors, the electrode material can influence the overpotential of some species in mixtures, in this way enabling the separation of two similarly oxidisable or reducible species, resolving some interference problems. The high overpotential for hydrogen
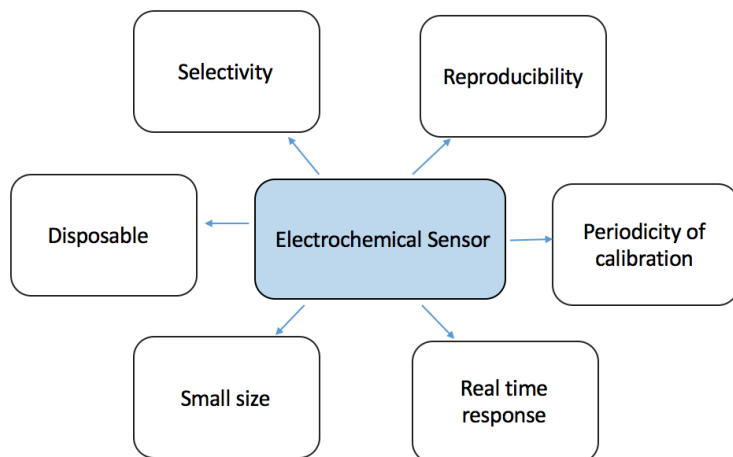
Figure 1.1: The advantage of electrochemical sensor.

evolution at mercury electrodes in aqueous solution is the most well-known example. – Each electroactive species undergoes reaction (oxidation or reduction) at a particular potential. Thus, an applied potential in voltammetric or amperometric sensors can lead to high selectivity and specificity, and enable probing of speciation (including different species in the same oxidation state). Few other analytical techniques have this possibility. – Since the signal obtained at an electrochemical sensor is electrical in nature (a voltage or a current), no further signal transduction is needed. Thus, with modern electronic circuitry, for voltammetric sensing, instrumentation can easily be adapted to apply complex applied potential waveforms and analyse the response using a variety of signal treatment software and chemometric tools, leading to sensors with high sensitivity and low detection limits.

Surface-modified electrode characteristics can be tuned through appropriate designs and architectures so that the electrode is itself both a reagent and a detector for electrochemical sensing. – Small, portable sensor systems incorporating the sensor itself and dedicated, battery-powered, instrumentation can be used outside the laboratory, particularly in situations where no pretreatment or sample digestion is needed. – Sensors can be easily miniaturised and incorporated in flow systems for online monitoring. A general limitation of voltammetric sensors is the requirement that sufficient, inert electrolyte needs to be present to carry the current between the working (indicator) and auxiliary electrodes. This means that electrolyte sometimes has to be added to analyte solutions, unless microelectrodes are employed, but this can often be done automatically in flow systems if necessary
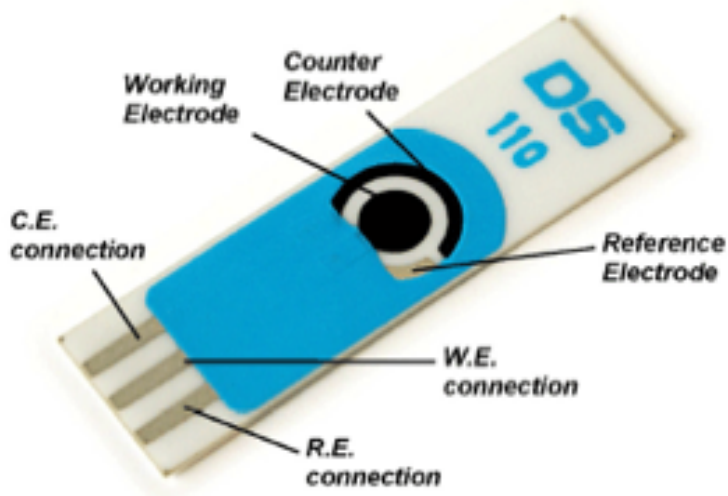
1.5. Screen Printed Electrode

Figure 1.2: Design of a disposable and portable screen printed electrode (with reference, working and auxiliary electrodes on the same substrate)

Nowadays, small, portable,fast, easy to use, disposable and economical electrode systems gradually substitute cumbersome electrochemical cells and bulky electrodes. Large amount of electrodes for outside and inside environmental monitoring has been developed during these years. Many outstanding examples, show the power, scope, versatility and application of such miniaturized electrodes for monitoring of environment are shown in the coming sections. Screen printing technique is very popular technique for the fabrication of electrochemical sensors. This methodologies are likely to underpin the progressive drive towards portable, sensitive, and miniaturized devices, and it have already achieved "lab-to-market" progress for different kinds of sensors. The development of application about these sensors for analysis of environmental are the major part of research recent year

Most of analytical research effort is poured to the development of robust and new methodologies. For example, new analytical tool is needed for real time monitoring of environmental pollutants, and for reduction of toxic materials in the environment. Progress is aimed to bring the data close to the production operations in the field of analytical chemistry. Such advance provide good analytical methods with reduction of environmental impact. Real time field detection systems are strongly desirable for continuous environmental detection to overcome the limitation such as transport to a central laboratory and sample collection problems associated with normal used methods for environmental pollutants. Electrochemical device has

special character to address the challenges of analytical chemistry. The advantages of electrochemical devices include portability and possibility of miniaturization , selectivity, sensitivity,a wide linear range, minimal space and power requirement. Electrochemical detection have been well established for many years. There were huge progress in electro-analytical chemistry with the appearing of tailored interfaces, ultra-microelectrodes, smart sensors and molecular devices. These developments have gained large popularity of electro-analyses and they will be applied into new environments and new phases.

1.5.1. Development of Screen Printed Electrode

The elimination of bulky materials and instruments from the analytical protocol is a major thrust of analytical chemistry. The performance of analytical methods is directly related to the material of the working electrode. With the advancements in electro-analytical science, various non-mercury. Recently, miniaturization of the solid electrodes was used to get several fundamental and practical advantages including such as a dramatic reduction in sample volume, portability and cost effectiveness. To address the needs of on-site analysis, it was necessary to move away from the commonly used cumbersome electrodes and cells. The exploitation of new fabrication techniques allows the replacement of bulky electrodes and conventional beaker type with easy to use sensors. Fabrication of printed devices on bendable substrates has enabled the development of a wide range of new electrode systems. Screen printing technology is a well established technique for the fabrication of economical, portable and disposable electrode systems. The whole electrode system, including counter, reference, and working electrodes can be printed on the same substrate surface. A promising commercialization of printed electrodes are the glucose sensor for diabetes[5] Society is in constant state of growth and development, and it is evident that demands for sensing devices related to the environment will increase with the passage of time. In order to achieve this, accurate, portable and rapid devices are highly needed. Decentralized analyses are necessary and thus traditional analytical methods cannot cope with these requirements.

1.5.2. Working Principle of a Screen Printed Electrochemical Sensor

Screen printed provide an feasible way to design new electrochemical sensors. low cost and reliable screen printed electrochemical sensors attracted scientists from wide range of fields. Basically, a screen printed electrode consist of substrate where three electrodes including reference electrode counter electrode and working electrode. All of these electrodes are printed through screen printing. The working electrode is the main electrode on which electrochemical reactions are occur, while the reference electrode and counter electrode are necessary so that to complete the measurement circuit. Figure 1.3 indicates the steps of fabrication of a screen printed electrode. The biological or chemical events on the screen printed electrode are

transfered into a detectable signal with the integrated transducer element. Among the different transduction techniques, the electrochemical method of detection are more successful and attracted more interest because the cost of devices are very low.
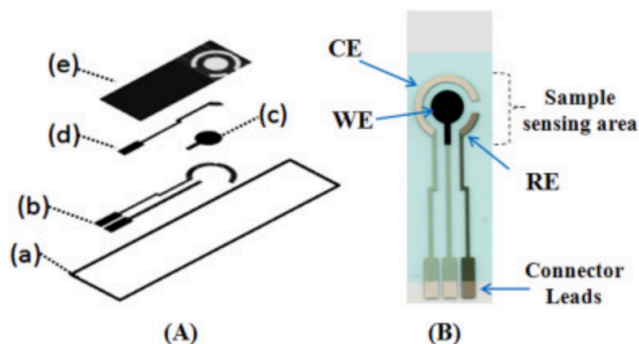

Figure 1.3: Fabrication of a three electrode system. Inert substrate; working and auxiliary electrode are screen printed; screen printing of reference electrode, protection paste; working electrode incubation with the analyte of interest

Usually, the fabrication for an screen printed sensor involves three steps: fabrication of the electrode, surface design and subsequently utilization for sensing applications.

1.5.3. Application to Biosensor strips

Electrochemical assays for determining the concentrations of enzymes or their substrates in complex mixtures of liquids have been developed. In particular, biosensor strips for biomedical applications (e.g., whole blood analyses) have been developed for the detection of glucose levels in biological samples. The biosensor strips consists of typical electrochemical cells where there can be counter electrodes, pseudo reference/counter electrodes and working electrodes. The potential of the working electrode is typically kept at a constant value relative to that of the pseudo reference/counter electrode.

Biosensor strips are used in the chemical industry, for example, to analyze complex mixtures. They are also used in the food industry and in the biochemical engineering industry. Biosensor strips are also useful in medical research or in external testing. In medical research, they can function as invasive probes (i.e., where they come into contact with a body fluid, such as whole blood or subcutaneous fluid). In external testing, they can function in a non-invasive manner (i.e., where they come into contact with blood withdrawn by a syringe or a pricking device).

A typical three-electrode sensor for blood analysis suitable for measuring the amount of analyte in a sample of liquid comprises (1) an active or

working electrode that is coated with a layer containing an enzyme and a redox mediator, (2) a passive or dummy electrode that is coated with a layer containing a redox mediator but lacking an enzyme, and (3) a pseudo reference/counter electrode or counter electrode. The redox mediator will transfer electrons in the catalyzed reaction when a liquid sample which contains catalytically active enzyme touch the electrodes. When a voltage is applied across the electrodes, a response current results from the reduction or oxidation of the redox mediator at the electrodes. The response current at the dummy electrode represents a background response of the electrode in contact with the sample. The response current at the working electrode is related to the concentration of the substrate. A corrected response current is calculated by subtracting the response current at the dummy electrode from the response current at the working electrode. This subtraction calculation substantially eliminates background interferences, thereby improving the signal-to-noise ratio in the sensor. When the resistance between the reference/counter electrode and the working electrode is large, Non-monotonic current decay will occur. This kind of current decay can make measurements of concentration of analyte complicate.

1.5.4. Traditional Lactate Sensor
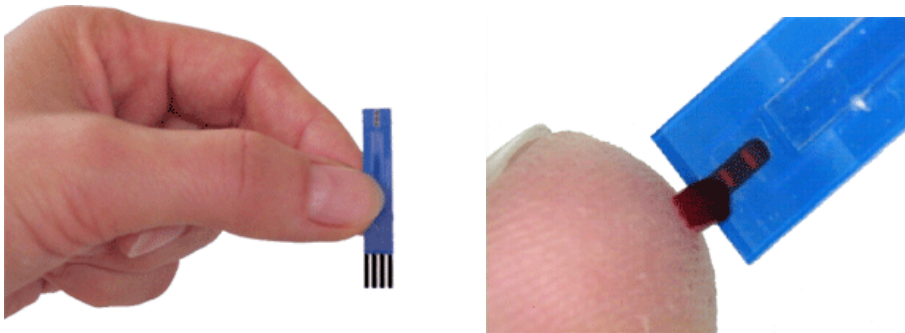
Figure 1.4: Product "Lactate Scout +"

Figure 1.5: This is measurement strip that can collect. blood sample. Correct why is holding strip so that the sensor connection is facing downward. The blood will be sucked into the monitor chamber through capillary action.

Nowadays, many lactate sensor used by clinicians around the world is invasive type as shown in Fig 1.5. This device is used for the easy and reliable measurement of lactate. Take popular lactate meter Lactate *Scout+* as a example. The way to get the sample properly is lowering the end of the inserted strip to a freshly created blood drop but avoiding direct contact with the skin surface. Then, the blood will be sucked into the monitor chamber through capillary action. Insert the test strip into the slot at the top of the Lactate Scout until is stops The arrow should face toward the

Figure 1.6: Insert the test strip into the slot at the top of the Lactate Scout unitl is stops The arrow should face toward the analyzer. When the analyzer is turned off, this auomatically turns the analyzer on and activates the measurement mode.

analyzer. When the analyzer is turned off, this automatically turns the analyzer on and activates the measurement mode. This kind of lactate meter was developed primarily for use in sports medicine but has found other applications within medical and veterinary medicine. The measurement system operates on the basis of enzymatic analyze and amperometric detection. Sample will have reaction with biochemical reagent on the surface of inserted sensor. Electrical signal that is created by this reaction is read by the device. This signal corresponds directly to the lactate concentration of the sample. lower the end of the inserted strip to a freshly created blood drop. Avoid direct contact with the skin surface. Through capillary action, blood can be absorbed into the chamber of monitor

1.6. MEMS Microelectrodes

Microelectrodes are defined as electrodes whose characteristic dimension is, under the given experimental conditions, comparable to or smaller than the diffusion layer thickness , which is commonly taken to be less than or equal to 50 µm. Theoretical modelling of processes at solid electrodes, which are usually flat, normally considers only semi-infinite diffusion perpendicular to the electrode surface. Nevertheless, if the electrode is reduced in size, then this becomes more and more important. Of course, modelling of the DME considered, to a first approximation, only spherical diffusion. The concentration gradient induced by spherical diffusion is much higher which has three consequences. First, a quasi-steady state is induced

Basically, microelectrodes can be embedded into human cells by the ultrafine tapered tip due to its small size. Tip of electrodes need to be small with respect to the size of human cell to prevent cell damage and it should

1

be strong enough to penetrate the cell wall. Due to its advantages that it can recording action potentials from single cells, it has been gain popularity in neurophysiological studies. Microelectrodes can clear up large amount of neurobiological problems. For example, with the technique called constant potential amperometry, the basics of vesicular release at the cellular level can be probed by microelectrodes [6] However, cyclic voltammetry is one of the primary alternatives to microdialysis to study neurobiology because it is less invasive when it is implanted and it has less enhanced temporal resolution[7]. Both techniques are significant for helping to understand of role in behavioral neurobiology and brain chemistry.

1.6.1. MEMS Lactate Sensor Designed by Fraunhofer Institut

Figure 1.7 is the lactate sensor designed by Fraunhofer. In Fraunhofer's design,a miniaturized sensor for continuous lactate measurement in saliva was developed and tested. The sensor was built using silicon microfabrication technologies. The size of the chip is 5.5 mm × 6.4 mm × 0.7 mm and features a working, a counter and an Iridium reference electrode. There is a cavity for the micro fabricated chip. The floor of cavity is punctured by fine pores. The cavity contains the enzyme lactate oxidase (LOD), which is immobilised in an agarose gel. Prior to the amperometric detection of the reaction product hydrogen peroxide at the working electrode, the analyte lactate has to pass the pores to reach the cavity with the lactate oxidase by diffusion. The miniaturized lactate sensor features a cavity in whose floor pores are etched. The sensor uses a three-electrode set-up. Inside the cavity is a platinum working electrode. The counter and reference electrode are also integrated on the sensor chip. The sensor uses the conventional principle of lactate oxidation via the enzyme lactate oxidase followed by electrochemical detection of hydrogen peroxide, as described frequently (e.g. Guilbault and Lubrano, 1973; Scheller and Schubert, 1989; Perdomo et al., 1999). In this case, the lactate oxidase is immo- bilised inside the cavity in a matrix of agarose gel. Then the top of the cavity is sealed by a self-adhering polyester foil. When the sensor chip is immersed into a solution containing lactate, a concentration proportional amount of lactate molecules will diffuse through the pores in the floor into the cavity where they are oxidised enzymatically to pyruvate. In a second reaction step hydrogen peroxide is generated and further oxidised elec- trochemically at the platinum working electrode. This enables amperometric readout of the lactate concentration. There are some disadvantages of lactate sensor design by Fraunhofer.

Figure 1.8 shows that the peak response current of this lactate sensor is around 300nA. Limited response current will reduce the sensitivity and stability of the sensor. Invasive sensing for blood lead to short life time of the sensor and do harm to human health for longtime use.
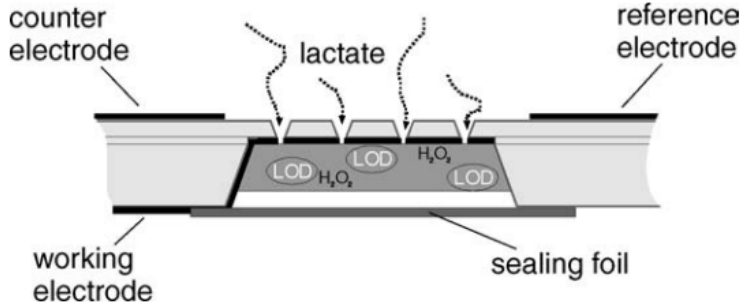
1

Figure 1.7: The plan view of the construction principle of lactate sensor[8]
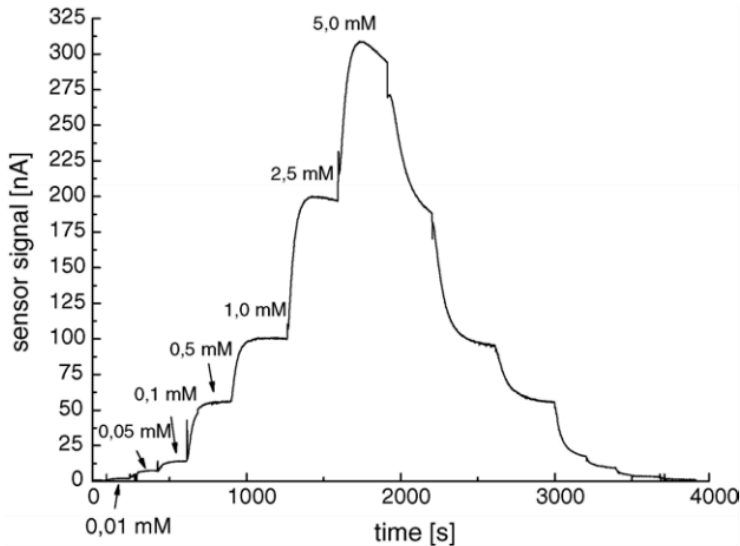

Figure 1.8: Amperometric response of a silicon to an increasing lactate concentration in PBS solution

1.7. Design of high aspect ratio MEMS electrochemical Sensor

In this project , the design and development of 3D electrochemical sensor with high aspect ratio is analysed. The sensor will be fabricated by MEMS technology and share the advantage of silicon micromachining technology deep reaction ion etching. Thus the surface area can be increased to 7 to 10 times as plain 2D sensor. The sensor is based on electrochemical sensor which has diffusion holes and enzyme cavity and need to be compatible with voltammetric measurement which contains three electrodes. The semiconductor manufacturing techniques ensure highly reproducible sen-

sor chips and provide the ability for mass fabrication. The pillar structure increase the aspect ratio so as the current. The sensor uses the common enzymatic and electrochemical principles and employs a diffusion limiting diffusion layer so that the sensor can work in the linear region. All necessary electrodes for a three-electrode system are integrated on the chip. The construction and the silicon micromachining of the sensor are presented as well as the sensor properties. Standardised V-I tests were employed.

1.8. Thesis Outline

The thesis writing consists of five chapters.
• Chapter 1: Introduction: Motivation, Focus of thesis work and Methodology.
• Chapter 2:Simulation: The simulation of aspect ratio, minimum thickness of electrode.
• Chapter 3: Fabrication : Fabrication process of electrochemical sensor
• Chapter 4: Process challenge and measurement result
• Chapter 5: Conclusion and future work.

2

Simulation

This chapter will focus on simulation of the aspect ratio and limitation of thickness of electrode. Equivalent model was built for easy calculation of the surface area of sensor.

2.1. Surface area analysis
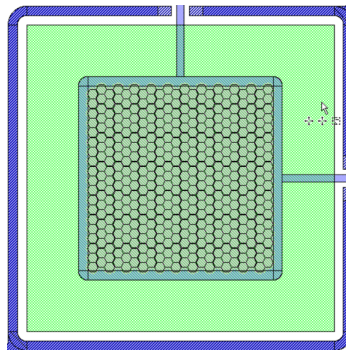
Figure 2.1: The plan view of the whole sensor

In order to get high aspect ratio structure sensor, we start simulation with pillar structure. Figure 2.1 show the sensor shape that will be fabricated in the processing. The ratio that how much surface area will increase because of adding of pillars will be show in the following calculation step. As shown in Figure 2.1, the whole sensor consists of 418 hexagons. The structure of every hexagons is identical. Therefore, the percentage of surface area that increased by pillar is exactly the same for every hexagons area and so as to the whole structure. So calculation of the increase in area of whole structure can be substituted by calculation the increasing

area and the ratio for only one hexagons.
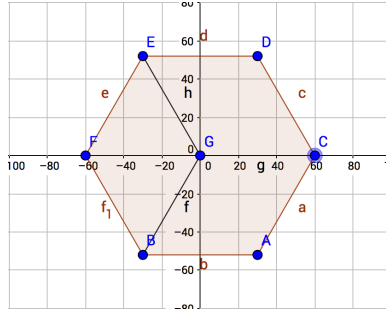
Figure 2.2: Bottom plane that is divided into three parts

If there is no pillar, the plane area can be calculated with the equations below:

$$A_1 = 6 \times (\frac{1}{2} \times a \times h) \tag{2.1}$$

$$A_1 = 6 \times (\frac{1}{2} \times a \times \frac{\sqrt{3}}{2} \times a) \tag{2.2}$$

$$A_1 = \frac{3\sqrt{3}}{2} a^2 \tag{2.3}$$

Where A_1 is the area of plane hexagons without pillars, a is the length of the hexagons, h is the hight of one small triangle in the hexagons. Taking Figure 2.2 as a example where a is 60um.

$$A_1 = \frac{3\sqrt{3}}{2} \times 60^2 \approx 9353 um^2 \tag{2.4}$$

Then, area of the plane with pillars will be calculated. As shown in Fig 2.2, whole the hexagon has been divided into 3 parts: GCDE, GEFB and GCAB. The number of pillars can be determined by figure 2.3

The number or pillars in each region can be counted. For this hexagon with 60um length, the number of pillars is:

$$N_1 = n_1 \times n_1 - n_2 \times n_2 \tag{2.5}$$

Where n_1 is the number of pillars on the edge lines of hexagon, $n_2 \times n_2$ in the equation means the number of pillars around diffusion hole region should not be counted.

So the total number of pillars can be calculated as below:

$$N = 3 \times N_1 - 3 \times (n_1 - n_2) \tag{2.6}$$
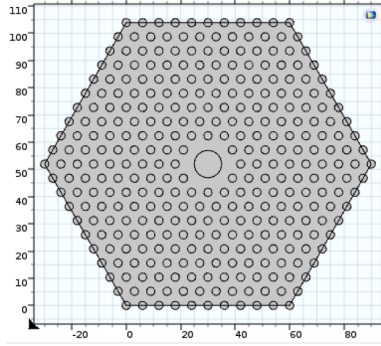
Figure 2.3: Top view figure of one unit hexagon with pillar

Where $3 \times N_1$ means there are three part of pillars and $3 \times (n_1 - n_2)$ means the lines of pillars that on the edge of there parts have been calculated twice, thus they should be subtracted here. Thus:

$$N = 3 \times (n_1 \times n_1 - n_2 \times n_2) - 3 \times (n_1 - n_2) \tag{2.7}$$

$$N = 3 \times n_1^2 - 3 \times (n_1 - n_2) - 3 \times n_2^2 \tag{2.8}$$

For this modal, n_1 is 11 n_2 is 2, thus

$$N = 3 \times 11^2 - 3 \times 9 - 3 \times 2^2 = 324 \tag{2.9}$$

After getting the number of pillars for one hexagon of this structure, the total area of this structure can be divided into two parts. Bottom plane A_b and pillars surface area A_p.

We get,

$$A_b = A_1 - N * \pi r^2 \tag{2.10}$$

$$A_1 = 3 \frac{\sqrt{3}}{2} a^2 \tag{2.11}$$

Where A_1 is the bare hexagon area got in (2.3)

$$A_p = 2\pi r * h * N + N * \pi r^2 \tag{2.12}$$

Hence, Total surface area of this unit structure is:

$$A = A_b + A_p = 3 \frac{\sqrt{3}}{2} a^2 + 2\pi r * h * N \tag{2.13}$$

$$A = 3 \frac{\sqrt{3}}{2} a^2 + 2\pi r * h * (3 \times n_1^2 - 3 \times n_1 - 3 \times n_2^2) \tag{2.14}$$

Take the sample shown in the Fig 2.3 as example, $a = 60um$, $r = 1.5um$, $h = 30um$, $n_1 = 11$, $n_2 = 2$ Total surface area of this unit structure can be got as:

$$A = 3 \times \frac{\sqrt{3}}{2} \times 60^2 um^2 + 2 * \pi * 1.5um * 30um(3 \times 11^2 - 3 \times 11 - 3 \times 2^2) \quad (2.15)$$

$$A = 9353^2 um^2 + 2\pi * 1.5um \times 30um \times 324 \quad (2.16)$$

$$A \approx 9353um^2 + 91562um^2 = 10092um^2 \quad (2.17)$$

Then, the aspect ratio that this structure increase can be got as:

$$R = A/A_1 = 100920/9353 \approx 10.79 \quad (2.18)$$

2.2. Thickness of electrode

In this thesis, study of TiN and platinum as working electrodes are done. Details of measurement result will be discussed in later chapter. For the process using platinum, thickness of platinum electrode is a important parameter which should be precisely calculated. The thickness need to meet the requirement which balance the cost of platinum and the surface resistance. Due to high cost of platinum, the thickness of metal electrode should be controlled. Otherwise this sensor is difficult to be commercialized. However, thinner thickness will lead to higher surface resistance of electrode. As discussed before, the excitation signal is varied linearly with time in Cyclic Voltammetric Study; first scan positively. Then the potential is scanned in reverse, causing a negative scan back to the original potential to complete the cycle. However, any electron flowing on surface will cause voltage difference on the surface of working electrode. Thus, the excitation signal of Cyclic Voltammetric measurement will become unstable because of this voltage difference and so as to output current.

The important parameters of a Cyclic Voltammetric plot are the anodic peak current $i_p a$, cathodic peak current $i_p c$, anodic peak potential $E_p a$, and cathodic peak potential $E_p c$. (For our case, pick current can be get when voltage is around 0.4V) which limit the voltage drop to 400uV between any point on the surface of electrode because relative error below 0.1% is needed for the supply voltage of the sensor. This voltage limitation will restrict the thickness of sensor surface to a certain value. For example, assume the maximum current that this sensor can get is 100uA. Then the minimum thickness of sensor can be get as follow: According to Ohm's law

$$dR = \frac{dV}{dI} \quad (2.19)$$

The resistance of a given object depends on two factors: What material it is made of, and its shape. For a given material, the resistance is inversely
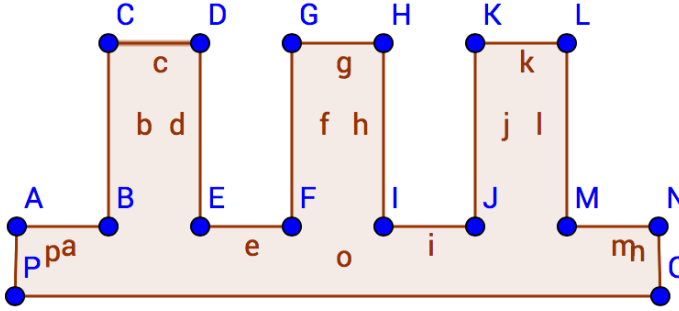
Figure 2.4: Front view of sensor - Vertical rectangles represent pillar structures

proportional to the cross-sectional area. Also, for a given material, the resistance is proportional to the length;

$$R = \rho \frac{l}{A} \tag{2.20}$$

where l is the length of the conductor, measured in metres [m], A is the cross-sectional area of the conductor measured in square metres [m²], and ρ (rho) is the electrical resistivity (also called specific electrical resistance) of the material, measured in ohm-metres (Ω·m).

As shown in Fig 2.4, there are only two types of surface voltage drop for this structure, one is caused by current go through the bottom plane and do not pass through pillars such as current go from A to B, and another voltage drop is caused by current go from the top of pillar to the bottom of pillar such as current go from point C to point B. One case need to mention here is: there is nearly no current that will go to any top of pillar again after it go down to the bottom of one pillar. This is because electrode takes the path of least resistance. When one path has much higher resistance, practically nearly all the current will flow through the other path. Therefore, the total voltage error caused by surface current can be counted as two part: voltage difference on bottom plane V_b, and voltage difference between top of pillar and bottom of pillar V_p. Maximum voltage difference:

$$V_{max} = V_b + V_p \tag{2.21}$$

Therefore, voltage related minimum thickness t_{min} can be defined.

$$V_{max} = I \times R_{max} \tag{2.22}$$

$$R_{max} = \rho \frac{l}{A_{min}} \tag{2.23}$$
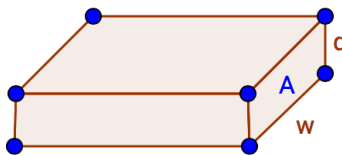
Figure 2.5: A square resistance model that can be used for calculate minimum thickness.

As we can see in the Fig 2.5

$$A_{min} = w \times d \tag{2.24}$$

d can be control by evaporation of platinum. So minimum thickness can be got from following equation:

$$V_{max} = I \times \rho \frac{l}{w \times d_{min}} \tag{2.25}$$

$$d_{min} = I \times \rho \frac{l}{w \times V_{max}} \tag{2.26}$$

From 2.26, we know the minimum thickness is related to the geometry of the structure, current, and maximum voltage error. Where I refer to the electron that is created by redox reaction. V_{max} is 400uV which is mentioned before. But for the geometry of the structure, it is really complicate to categorize and use it to calculate the I-V property. So, Here we use comsol to do the simulation.

Here we use Electroanalysis Model in Comsol because this model has the equations, boundary conditions, and rate expression terms for modeling mass transport of diluted species in electrolytes using the diffusion-convection equation, solving for electroactive species concentrations. The physics interface contains tailor-made functionality for modeling cyclic voltammetry and electrochemical impedance spectroscopy. This model meet our requirement that simulation of electrical property between diluted species and metal is easy.

For our simulation, we start geometry building as the Fig 2.6 shown below. This is the same basic structure as we calculate the aspect ratio which has side length of 60um, diffusion hole with radius of 6um and 324 pillars whose radius are 3um and height is 20um. Simulation purpose is to calculate minimum thickness which is relate to maximum voltage pulses. Maximum voltage pulse is caused by flowing of electron on surface. Therefore, the moment that electron flowing through the longest path between two pieces is chosen. Because for our device, width(w) is fixed and I is chosen in a certain moment when V_{max} occur. Assume it is ideal situation that
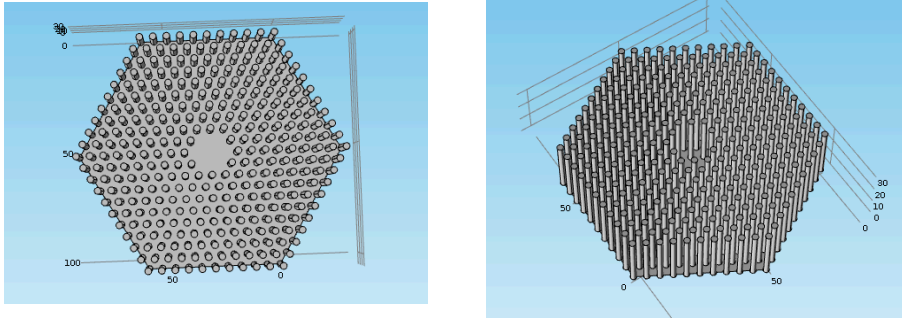
Figure 2.6: One basic hexagon of sensor structure with the same dimension of the hexagon structure mentioned before when aspect ratio is calculated. The side length is 60um and it contain 324 pillars whose height is 30um, ratio is 1.5um.

all electron created by redox reaction are captured by working electrode and no other electron loss because of other chemical reaction.

The advantage of the comsol model is it can calculate any voltage between two point of your design, only if boundary conditions are given.

In order to calculate the voltage drop of the whole sensor surface, sensor strcuture shown below should be simplified. From the geometry of the sensor structure below, we can see the sensor is made of 418 hexagons. If we want to get the surface voltage drop of the whole structure, we can start from one hexagon.
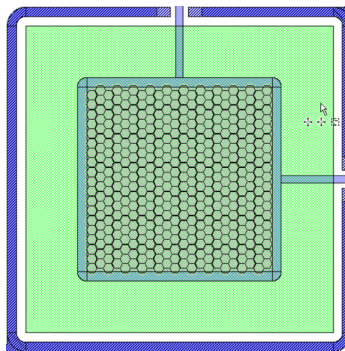
Figure 2.7: The plan view of the whole sensor

Here we choose one hexagon of a mask as show in Fig.2.8 below(2D Plan view) which is the same model as we calculate the aspect ratio in previous section. Hence, the number of pillars (N) for this structure is 324. Assume the electron which is created by redox reaction is on the surface of electrode equally.

The model can be simplified to a plane hexagon as shown on the right. We want to get the voltage difference from point(60,0) to point(0,60*sqrt(3))

because this is longest way that pass through the structure. As mentioned in 2.21, this voltage can be separated to two part: voltage drop of one pillar and voltage drop of the plane between this two point.
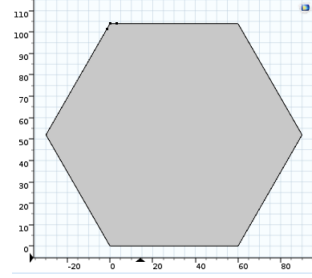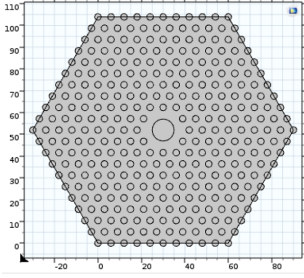
Figure 2.8: Plan view of one hexagon will pillars on top of it.

Figure 2.9: Plan view of simplified model of one hexagon without pillar

Now we do the simulation in the comsol. This comsol model assume:

$$\nabla \cdot J = Q_j \tag{2.27}$$

$$J = \sigma E + J_e \tag{2.28}$$

$$E = -\nabla v \tag{2.29}$$

The advantage of this comsol model is that we can get voltage between any two points as long as we know the current density and the boundary condition.

All the parameters in our model are given below: Current here is 1uA

Parameter names	Definitions
a	Length of the hexagon ($60um$)
I	Current of the sensor($1E-6A$)
d	Thickness of the electrode (it is variable from 1nm to 10nm)
s	Area of the hexagon($100920 \times 10^{-12} m^2$)
Qj	Current density of the surface($variable\,according\,to\,thickness$)

Table 2.1: Simulation parameters

because it is the goal that we want our sensor can reach. The surface area of one hexagon of the structure is:

$$S = S_{bottom} + 324 * S_{pillar} = 100920 \times 10^{-12} m^2 \tag{2.30}$$

The current density is

$$Q_j = I/V \tag{2.31}$$

$$V = S * d * 418 \tag{2.32}$$

$$Q_j = I/(S * d * 418) \tag{2.33}$$

For the whole structure, there are 418 hexagons and we assume that the electrons created by redox reaction will be distributed to the whole structure evenly. The result of this simulation show the voltage distribution on one hexagon structure when electron are captured by it. The current density has been calculated before in (2.33). The only variable thickness (d) of the structure can be changed which means we can get different voltage distributions from different thickness. In order to simplify the model, we set potential one length of hexagon to be zero as boundary condition. The result of this simulation show as Fig2.10 below
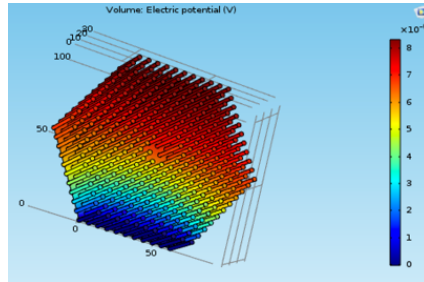
Figure 2.10: The plan view of the whole sensor

In this figure, we can see different colors which represent different potential. The value of potential are indicated in the right legend. Therefore, red regions in this structure have highest potential around $8 \times 10^{-6}V$ and blue regions in this structure have lowest potential around 0V.

As we mentioned before different thicknesses have different voltage distributions. Here we show the table that list the different voltage distributions correspond to different thickness. We only pick the largest potential in one distribution because our purpose is to find the lowest thickness that limit the surface voltage pulse to 400uV(control error to 0.1% of supply voltage which have been mentioned before)

This simulation is only for one basic hexagon. As Fig 2.16 show, there are 29 identical hexagons on the longest path of the surface of the sensor structure. The voltage listed in the third column of table 2.2 is the largest voltage pulse of the whole sensor. It is 29 times larger than the voltage error of one hexagon. From the table 2.2, we can roughly conclude that the largest voltage pulse will decrease as the thickness become thicker. In order to visualize the result, we make a graph of this table and do the curve fitting as Fig 2.12 follow:

The equation of curve is:

$$y = 2313.3x^{-0.985} \tag{2.34}$$

The fitting coefficient $R^2 = 0.99986$ which means the fitting is very good.

d(um)	V(3D)(uV)	29*V(3D)(uV)
1	79,4	2302,6
2	40,1	1162,9
3	27,2	788,8
4	20,4	591,6
5	16,5	478,5
6	13,7	397,3
7	11,8	342,2
8	10,3	298,7
9	9,2	266,8
10	8,1	234,9

Table 2.2: List of the largest surface voltages with different thickness
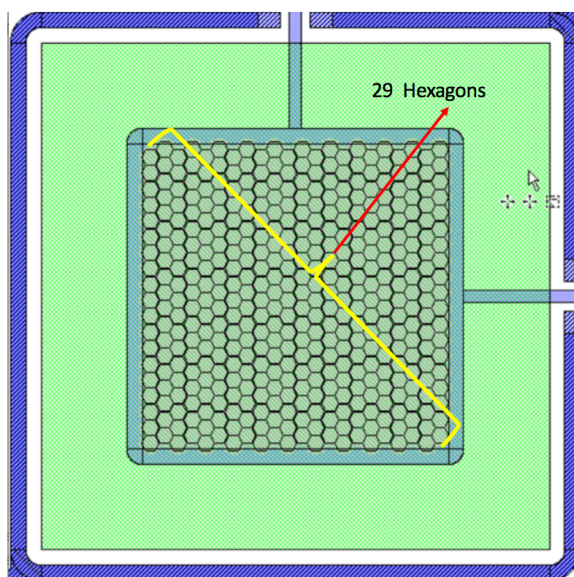
Figure 2.11: 29 hexagons along the longest line of sensor.

so we can calculate the thickness when surface voltage is 400uV by using formula (2.34).

$$400uV = 2313.3 \times d^{-0.985} \tag{2.35}$$

$$d = \sqrt[-0.985]{400uV/2313.3} = 5.94um \tag{2.36}$$

2.3. Model Simplification

The simulation of the pillars are time consuming because the working electrode is too thin. Thin layer around 1nm require the minimum element size
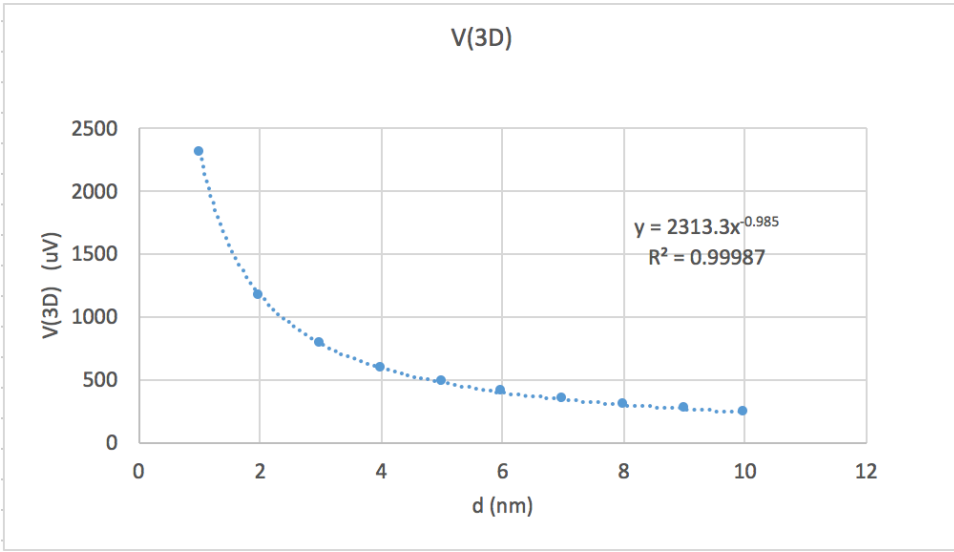
Figure 2.12: Voltage error due to the current flow on the surface of the sensor

of mesh for this structure to be less then 1nm. In comsol, such element size lead to huge data (60Gb) processing for whole structure. So we simplify the model to equivalent model who has the same electrical behavior. Because electron only flow in the working electrode layer, the inside pillars are electric insulation. So we only build platinum pillars who are smaller rather than insulating pillar with platinum covered outside. As long as the volume of equivalent pillars being the same with working electrode layer in the previous model, the electric behavior will be the same. The equivalent volume of pillar in the new model is:

$$V = d * S \tag{2.37}$$

Where d is the thickness of working electrode and the S is the surface area of one pillar.

Then the radius of new pillars can get by the equation below:

$$(2 * \pi * r_1 * h + \pi * r_1^2) * d = \pi * (r_2)^2 * h \tag{2.38}$$

$$r_2 = \sqrt{\frac{(2 * \pi * r_1 * h + \pi * r_1^2) * d}{\pi * h}} \tag{2.39}$$

For the structure with 1.5um radius, and 30um height and 1nm thickness, the radius of new pillars is:

$$r_2 = \sqrt{\frac{(2 * \pi * 1.5 * 30 + \pi * 1.5^2) * 0.001}{\pi * 30}} = 0.554um \tag{2.40}$$

Because building 3D models of this structure is really complicate. Building it for every size of samples is time consuming. And running 3D model in comsol is very slow. So we make a equivalent 2D comsol model. As we mentioned before in (2.21) , surface voltage can error can be caused by two situation: one is the voltage caused by current which is flowing through the bottom surface and the other is voltage caused by current which is flowing through side wall of pillar. Here we do two simulation separately. All the voltage causing by flowing electrode on pillar can be seen as small voltage(comparing to voltage caused by flowing on bottom surface).

The side length of bottom hexagon is 60um which is the same with the 3D model. and the pillar height is 20um. The total current of this equivalent model should be the same with the 3D model.

we can do simulation separately and the results of two part are listed in the table below:

V_p in this table means the voltage error caused by flowing current on pillar and V_b means voltage error caused by flowing current on bottom plane and the result on table have already times 29 because for the whole structure, there are 29 hexagons on the longest path. Because we transfer a 3D model to a 2D model in geometry, we here assume the current density do not change in this 2D model. And we assume the shape of 2D model is hexagon too. Equivalent area in 2D model is the total surface area of 3D model

$$A = 70425 \times 10^{-12} m^2 \tag{2.41}$$

Than we can get the side length of new hexagon of this 2D model

$$S = 6 \times \frac{\sqrt{3}}{4} a^2 = 70425 \times 10^{-12} \tag{2.42}$$

$$a = \sqrt{\frac{\frac{S}{6}}{\frac{\sqrt{3}}{4}}} = 165um \tag{2.43}$$

As shown in second column of this table, the voltage error caused by the current flowing on pillar is very small when comparing it to the voltage error caused by bottom.

$$r = \frac{V_p}{V_b} = \frac{A}{B} \times \frac{10^{-9}}{10^{-6}} = \frac{A}{B} \times \frac{1}{1000} \tag{2.44}$$

$\frac{A}{B}$ is constant, thus

$$r = \frac{V_p}{V_b} << 1 \tag{2.45}$$

From (2.38) above, we can conclude that V_p is negligible when voltage error is calculated in this equivalent model

$$17.1 \tag{2.46}$$
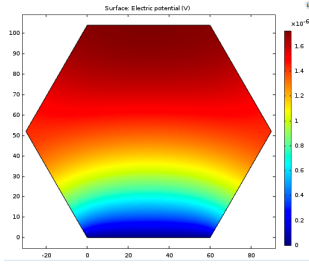
Figure 2.13: Simulation result of voltage drop in on the plane
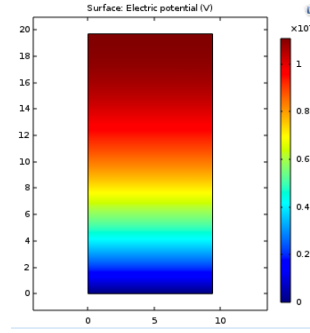
Figure 2.14: Simulation result of voltage drop in one pillar

d	V(p)	V(p)*324	V(b)	V(2D)	29*V(2D)
1nm	0,11	35,64	17	52,64	1526,56
2nm	0,085	27,54	8,6	36,14	1048,06
3nm	0,057	18,468	5,7	24,168	700,872
4nm	0,042	13,608	4,2	17,808	516,432
5nm	0,034	11,016	3,4	14,416	418,064
6nm	0,028	9,072	2,8	11,872	344,288
7nm	0,024	7,776	2,4	10,176	295,104
8nm	0,021	6,804	2,1	8,904	258,216
9nm	0,019	6,156	1,9	8,056	233,624
10nm	0,017	5,508	1,7	7,208	209,032

Table 2.3: Table of voltage error caused by pillars

Table 2.3 lists the surface error caused by pillars and bottom plain. Where V_p is voltage error caused by one pillar. There are total 324 pillars for one hexagon, column three of Table 2.3 list the voltage error caused by total 324 pillars. V_b is the voltage error caused by bottom plain and V_{2D} is the sum of total error the total error caused by whole structure in 2D model. V_{2D} is:

$$V_{2D} = V_t = V_b + 324 \times V_p \tag{2.47}$$

The same with V_{3D}, V_{20} need to be time 29. The trend line of V_{2D} is figure 2.15

Fitting formula of 2D model is:

$$y = 1748.6x^{-0.905} \tag{2.48}$$

The fitting coefficient $R^2 = 0.98912$ which means the fitting is very good.
so we can calculate the thickness when surface voltage is 400uV by using formula (2.34).

$$400uV = 1748.6 \times d^{-0.905} \tag{2.49}$$

2
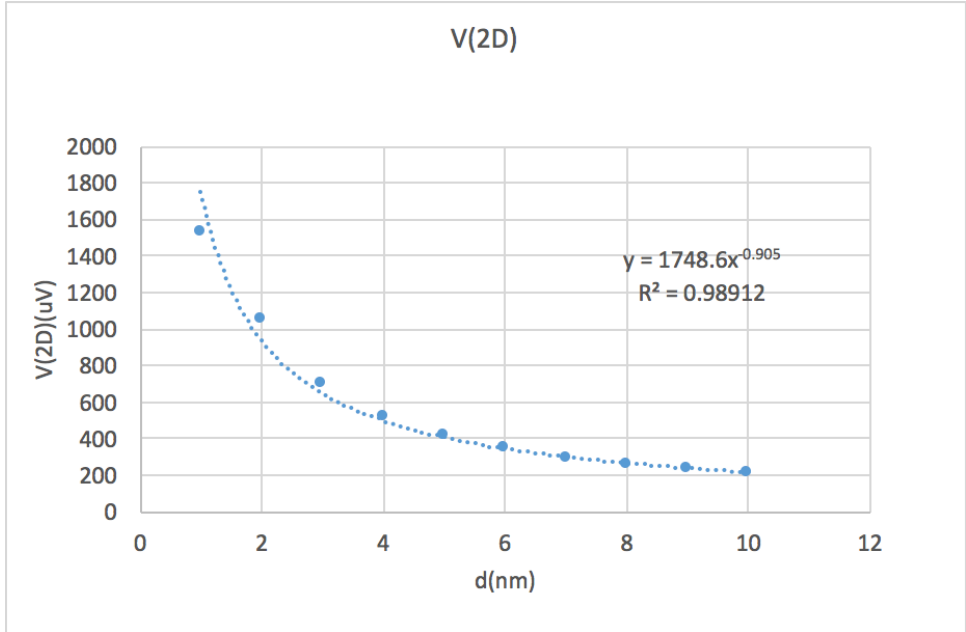
Figure 2.15: Voltage error due to the current flow on the surface of the sensor

$$d = \sqrt[-0.905]{400uV/1748.6} = 5.103um \tag{2.50}$$

The error of 2D model against 3D model is:

$$V_e = \frac{(5.94um - 5.103um)}{5.94um} \times 100\% = 14.1\% \tag{2.51}$$

The comparison of results between 2D model and 3D model is in Table 2.4.

Figure 2.4 shows, the surface voltage error of 2D model is reliable when the thickness of Pt larger than 2nm. The formula of linear regression are shown below.

sum of squares for error:

$$SSE = \sum^{i}(y_i - \hat{y}_i)^2 \tag{2.52}$$

Total sum of squares :

$$SST = \sum^{i}(y_i - \bar{y})^2 \tag{2.53}$$

d(nm)	29*V(2D)(uV)	29*V(3D)(uV)
1	1526,56	2302,6
2	1048,06	1162,9
3	700,872	788,8
4	516,432	591,6
5	418,064	478,5
6	344,288	397,3
7	295,104	342,2
8	258,216	298,7
9	233,624	266,8
10	209,032	234,9

Table 2.4: Comparison of V_{3D} and V_{2D}
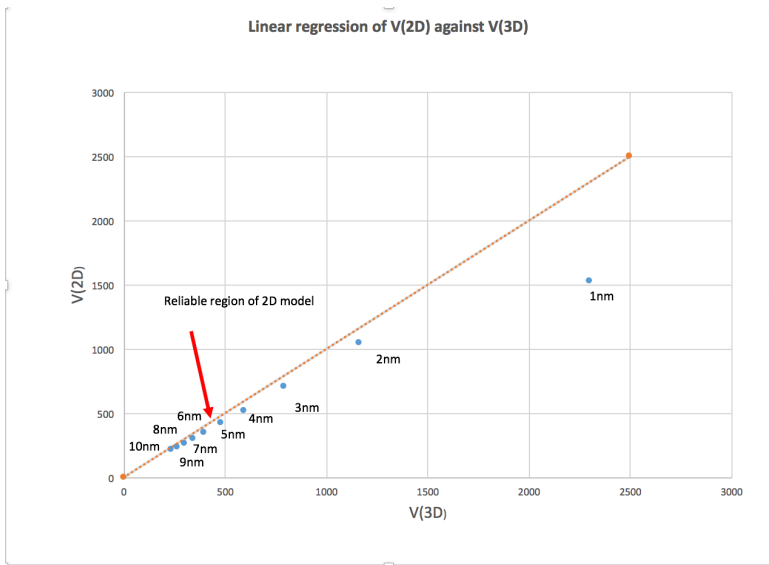
Figure 2.16: The linear regression of 2D model against 3D model

Regression coefficient R^2 is :

$$R^2 = 1 - \frac{SSE}{SST}$$

(2.54)

For the surface voltage error between 2nm to 10nm of Pt, the regression coefficient R^2 is 0.96217. It means the 2D model is reliable between the 2nm to 10 nm thickness of Pt.

3

Fabrication Process

In this chapter, details of fabrication of high aspect ratio sensor structure are presented. Three processing flowcharts are described. In the first two process flow, the structures are designed in the stepper mask. Two kinds of metal are used as working electrode in this processing: TiN, and platinum. In third run of fabrication, the working electrode and connector are designed in the wafer level using contact aligner masks.

All the processes of our sensors are finished with clean room fabrication compatibility and all of these processes are repeatable. The fabrication devices are demonstrated, followed by discussion and realization about improvements on fabrication technology.

3.1. DRIE etching

DRIE etching is the shorthand for deep reactive ion etching. By this etching method, micro-fabrication of many high aspect ratio structures(HARS) on silicon can be realized. HARS permit the fabrication of silicon able to range from 100um to 1000um. HARS make possible the fabrication of structures which are compliant in the plane of wafer but it will only be rigid in the direction normal to its surface [9]. Many promising and novel applications such as Gas Turbines, Rocket Engines and Power MEMS and be realized by the combination of HARS and aligned silicon wafer bonding[9]. Most of these applications need strict requirement such as high silicon etching rate, good selectivity to mask , compatibility with other processes on HARS.

3.1.1. THE BOSCH PROCESS

These high-density plasma tools can use two distinct gas-feeding approaches: standard and time multiplexing. The standard approach, all gas species are flowed at the same time, and the etching results depend on the glow discharge having both one species of radicals to proceed with the etch, and

another species of radicals for protecting the sidewalls during operation. In the time-multiplexing scheme, the etching and passivating gases used are flowed independently one at a time (see figure 2), and the machine alternates between an etching cycle and a passivating cycle.
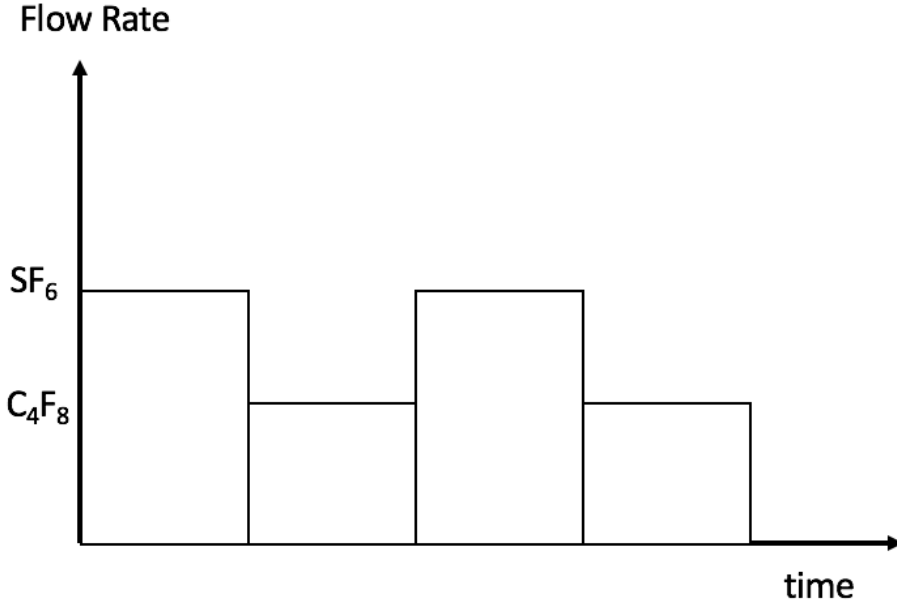
Figure 3.1: During TMDE a single gas species at a time is flowed into the reactor, first SF_6 for etching and subsequently C_4F_8 for sidewall passivation. The overlap between the etching and passivating cycles originates in the finite time response of the mass flow controllers. Typically the duration of the etching and passivating cycles is $\leqslant 12s$ and $\leqslant 10s$, respectively

During the etching cycle step a shallow trench is formed in the silicon substrate, with an isotropic profile characteristic of fluorine-rich glow discharges. The typical duration of these steps is ≤12s. During the passivation cycle, a protective fluorocarbon film is deposited on all surfaces. The duration of the step is usually ≤10s and shorter than the etching cycle. In the subsequent etch step, ion bombardment promotes the preferential removal of the film from all horizontal surfaces, allowing the profile to evolve in a highly anisotropic fashion (see figure 3). This separation of etching and passivating cycles is known as the Bosch process, after the German company that developed and patented this technique. In a typical configuration sulfur hexafluoride (SF6) is flowed during the etching cycle and octafluorocyclobutane (C4F8) during the sidewall protection cycle.

This process, succinctly described as time-multiplexed deep etching (TMDE), offers the advantage of exploiting the high silicon etching rate of fluorinated chemistries, such as SF6. For all practical purposes, TMDE users have to
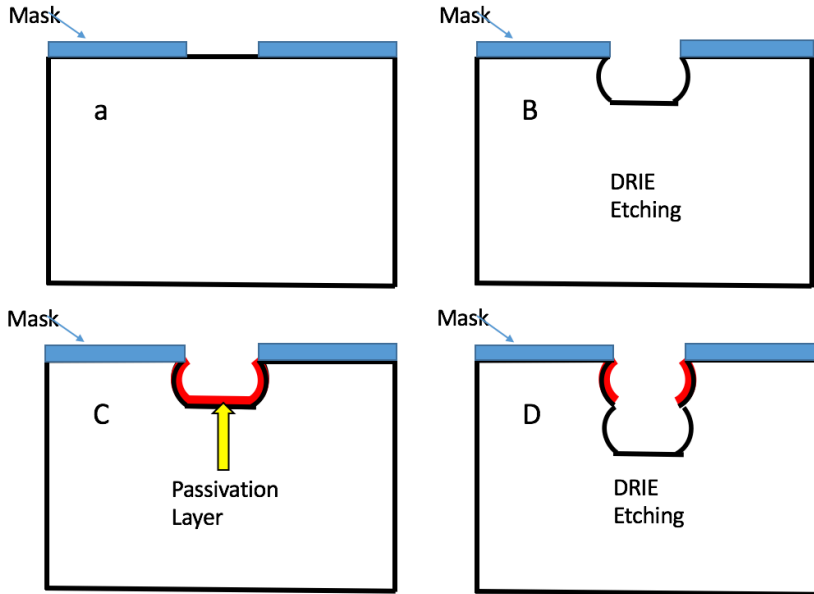
Figure 3.2: Cartoon showing the sequential steps during TMDE. In (a) the masking material (photoresist or silicon dioxide) has been patterned. During the etch step in (b), a shallow, isotropic trench is formed. In the subsequent passivation step(c), a protective fluorocarbon film is deposited everywhere. During the next etch step(d), the fluorocarbon film is removed from all horizontal surfaces by directional ion bombardment, and another shallow trench is formed.

deal with to different glow discharges: one for silicon etching and another for sidewall passivation. TMDE tools can also be operated in a continuous mode flowing only SF6 or C4F8. Fully isotropic profiles can be obtained using only SF6, with silicon etching rates in excess of 6 µm/min and selectivity to soft photoresist masks larger than 150:1. This fluorine-rich, high-density plasma has been exploited for etching structures without stringent profile requirements. Similarly, by using only a continuous C4F8 glow discharge, low surface-energy, pinhole-free, fluorocarbon films with various mechanical, optical and electrical characteristics can be deposited. The list of application for such films is very large: for orienting liquid crystal, as anti-corrosion films, as solid lubricants and for anti-stiction purposes. Their low dielectric constant can be exploited in tuning and resonant circuits or, in conjunction with high-conductivity metals, to realize electrical circuits with low RC-constants. Because of their low conductivity, fluorocarbon films are also applicable as electrical insulators. These films can be used as anti-reflection coatings, and, under specific deposition conditions, they can also serve as scratchresistant films. The high silicon etch-

ing rate of TMDE, combined with the possibility of employing soft masking materials, for instance photoresists, and the ability to control the profile of etched devices, provides another alternative for producing high-aspect-ratio structures (HARS). Compared with LIGA (German acronym for lithography-electroplatinginjection-molding), for instance, TMDE not only does not require a synchrotron radiation source, but it is also more compatible with integrated circuit technology and other cleanroom micro-fabrication process. LIGA, however, offers characteristics not surpassed by any other technology, namely, the production of metallic structures with the highest aspect ratio and with reasonably smooth surfaces.

3.2. Mask Preparing
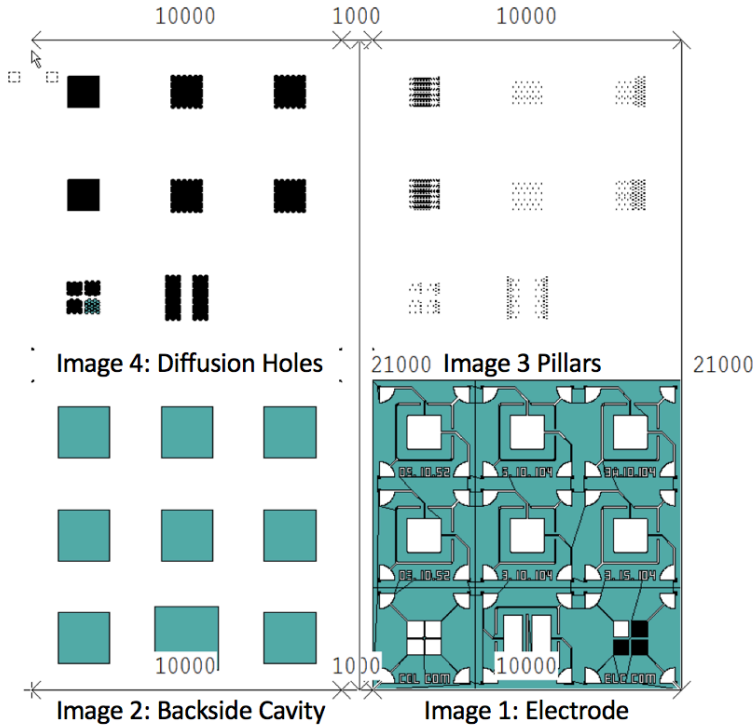
Figure 3.3: Standard 4 Images Mask

Standard 4 images mask is used for etching in processing. The size of each Image is 10um×10um. As the Fig3.3 show above, Image 1,2,3,4 correspond electrode layout, backside cavity, pillars and diffusion holes respectively.

3.3. Fabrication Process Flow Charts
3.3.1. Process Flowchart One
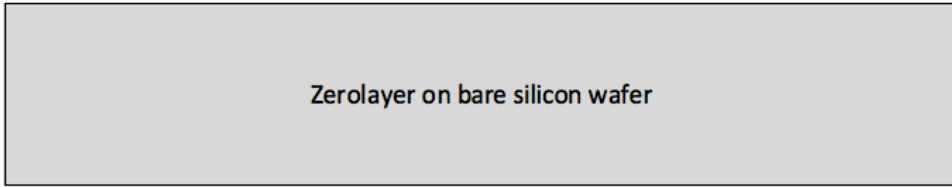
Figure 3.4

In the first step, a zero layer is etched in a 500um double side polished wafers as shown in Fig.3.4. Both N type and P type wafer are suitable because the type of silicon do not influence the distribution of the surface current so that the type of silicon dose not effect the final current signal of sensor. In the final sample, the output C-V property that need to be measured is only relate to the surface working electrode. The current is determined by surface area of electrodes, material of electrodes and concentrations of solution that used for testing. Details of sensor current and test solution will be discussed in next chapter of Measurement. In this step, standardized zero-layer process is done which use coating recipe Co-SPR 3012-1400-zero-layer in EVG120. Exposure is done by Stepper with the recipe comurk0.0 and energy $E = 120mJ$. Recipe $DEV - SP$ is used to do the development in EVG120.
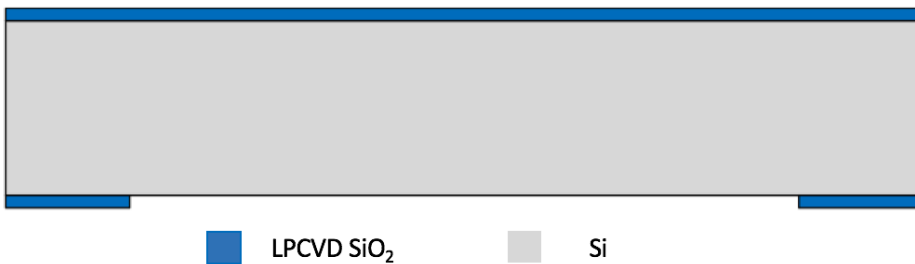
Figure 3.5

In Fig.3.5 , SiO_2 is deposited on both front side and back side of the wafer. Using furnace C1 to do LPCVD (Low pressure chemical vapor deposition) with recipe WetOxide. Expected thickness is 500nm. The deposition time can be got from Oxide-Growth Calculator. Figure below is the result of trend line of wet oxidation growth.

From the Figure 3.6, we can get oxidation time $0.64hour = 38.4min$. This
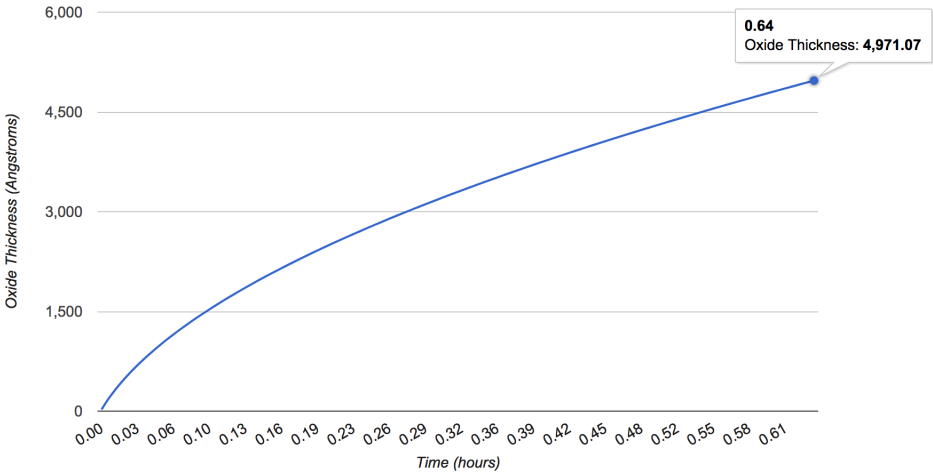
Figure 3.6: Thermal Oxidation thickness vs time

oxidation trend line is derived from formula below:

$$X(t) = \frac{A}{2}[\sqrt{\frac{t}{t_c} + 1} - 1]$$ (3.1)

In the figure 3.5 , backside SIO_2 has been etched so that there is a large trench. The SiO_2 is etched by Drytek Triode 384T plasma etcher with recipe "STDOXIDE" and etching time 100 seconds. This etching time is depend on etching rate of SiO_2 of Deytek which is around 6.9nm per second. Over etch is allowed in this step because the recipe of etching SiO_2 will almost not etch Si. In later step, this backside SiO_2 trench will serve as a hard mask for wet etching of backside cavity.
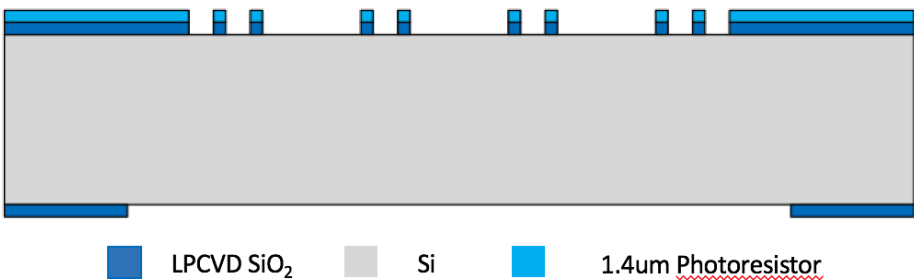
Figure 3.7

As for the front side, SiO_2 is serve as a hard mask for etching of pillars.

The etching of SiO_2 use the same method of etching hard mask of back side cavity using Drytek. In Figure 3.7 a light blue layer is on the top of SiO_2. This is a 1400nm photoresister layer which is used for etching the SiO_2 hard mask. This step using recipe "$Co\_3012\_1400\_NO\_EBR$" of EVG120 for coating. Exposure is done by Stepper with job named "10×10 die-4 image". Recipe "Dev-sp" is used for developing.

LPCVD SiO$_2$ Si   3um Photoresistor
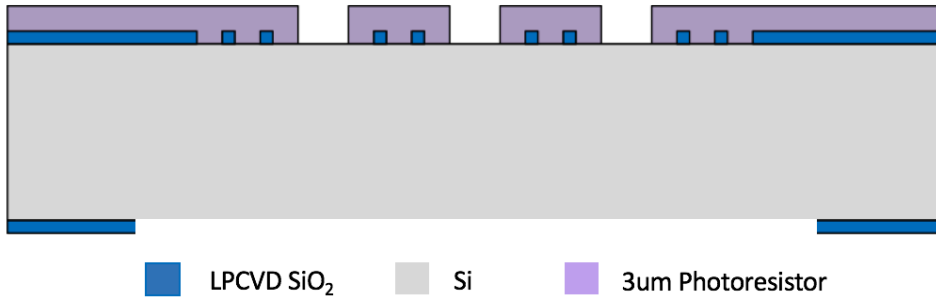
Figure 3.8

Fig.3.8 show a 3000nm photoresister on the top of SiO_2 which is for etching of diffusion hole. The recipe of it is $Cotopo2037\_NO\_EBR$. Standardized exposure and Development steps is used.

LPCVD SiO$_2$ Si   3um Photoresistor
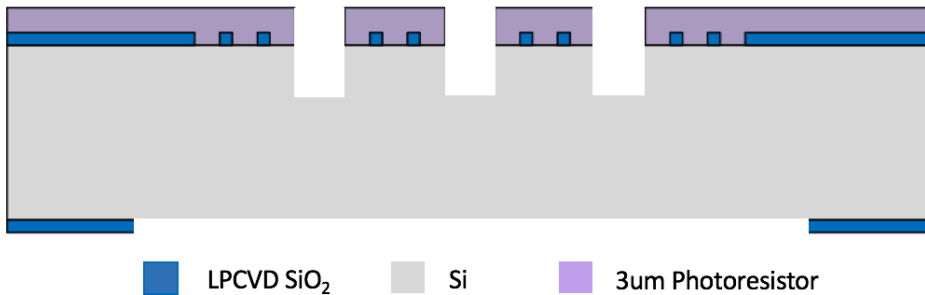
Figure 3.9

Etching of diffusion is in Edicson, temperature is set to $-10^o C$ because side wall need be protected very well otherwise sidewall will not be straight. Etching time is 15 minutes in order to get 40um depth diffusion holes.

Fig.3.10 show the step of etching pillar structure by Edicson. Temperature is also $-10^o C$ as mentioned before and etching time is 7 minutes 30 seconds for the aim of getting 20um pillars. Detail of problem met in this step will be discussed in later section.

Fig 3.11 show a deposition of LPCVD $TEOS$ on front side above pillar structure. Here, SiO_2 is chosen as a protecting layer on front side on the
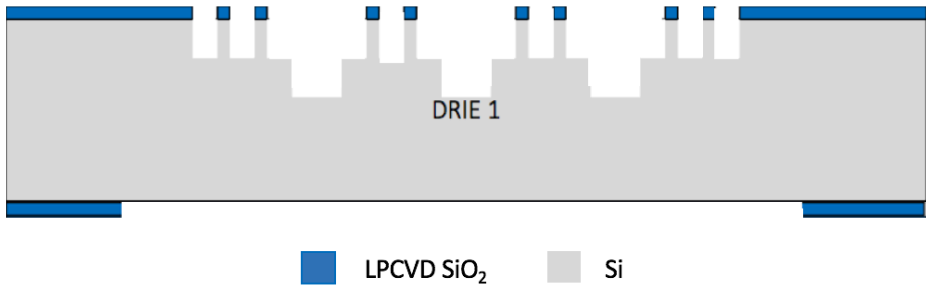
Figure 3.10
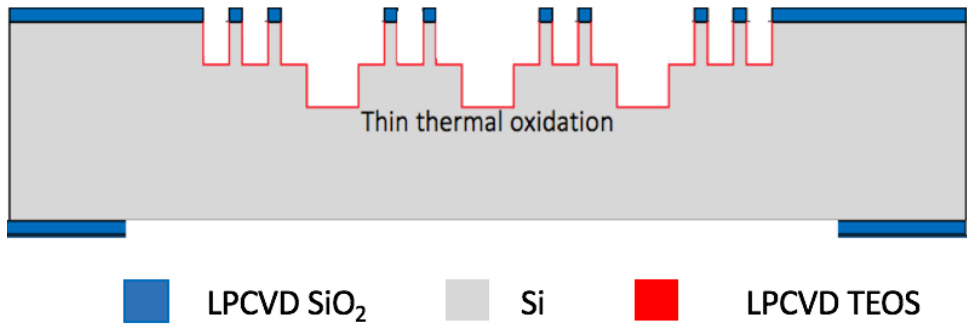
Figure 3.11

pillars structure when backside of wafer is etched by TMAH. Because pillars structure must not be destroyed by TMAH.
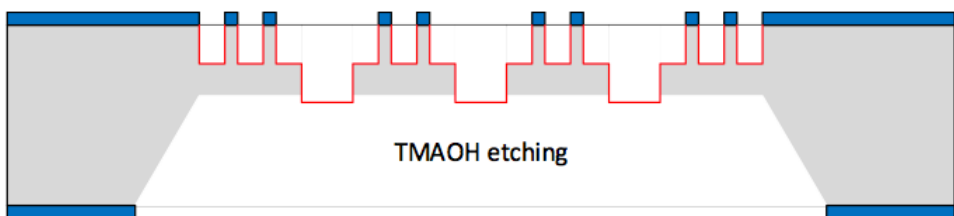
Figure 3.12

TMAH wet etching for backside cavity is chosen because it is quick and the shape of back side is not so important. The aim of this step is to etch through diffusion hole. As we can see in thi Fig 3.12 the sidewall of backside cavity is along the direction of 45° because TMAH wet etching is isotropic etching and it will etch alone the 111 crystal line.

The etching depth of cavity on the backside of wafer is:

$$D_c = T_w - D_p - D_d \tag{3.2}$$

Where T_w is the thickness of the wafer, D_p is the depth of etching of the pillars, D_c is the depth of etching of backside cavity and the D_d is the depth of etching of diffusion hole. For example, we use 500um thick wafer, pillars height is 30um and diffusion holes depth need to be etched in front side is 20um. Final depth of backside cavity is:

$$D_c = 500 - 30 - 20 = 450um \tag{3.3}$$

	EDP	KOH	TMAH
Si etch rate $[\mu m/min]$	0.75 to 1.25	1 to 2	≈ 1
SiO$_2$ etch rate [nm/min]	1 to 80	1 to 10	0.05 to 0.25
Si$_3$N$_4$ etch rate [nm/min]	0.1	very low	0.05 to 0.25
(100)/(111) etch ratio	35	400	10 to 35
Si roughness	low	very low	moderate
Al selectivity	no[1]	no	yes[2]
Au selectivity	yes	yes	yes
p^{++} etch stop $[cm^{-3}]$	B>7x10^{19} $\hookrightarrow$ER/50[3]	B>10^{20} $\hookrightarrow$ER/20	B>2x10^{20} $\hookrightarrow$ER/40
Alkali ions ?	no	yes	no
Cost	high	low	moderate
Disposal	easy	difficult	moderate
Safety	low	moderate	high

(1) One specific fomulation does not attack Al
(2) If specific amounts of silicon are dissolved in the etching solution
(3) Silicon etch rate divided by 50 if Boron doses higher than 7x10^{19}cm^{-3}

Figure 3.13: Table of selectivity of different materials when doing wet etching[10]

Table3.13, show that the etching rate of Si in TMAH is $1um/min$ and the etching rate of SiO_2 0.05nm/min to 0.25. Let us assume the SiO_2 is etched under maximum etching rate 0.25nM per minutes so that to ensure when the etching of backside cavity finish, front side pillars will not be destroyed. The thickness of SiO_2 can be derived from the equation below:

$$t = \frac{D_c}{R_{Si}} = \frac{D_{SiO_2}}{R_{SiO_2}} \tag{3.4}$$

Where R_{Si} is the etching rate of Si in TMAH, R_{SiO_2} is the etching rate of SiO_2 in TMAH. Then the minimum thickness of front SiO_2 is:

$$D_{SiO_2} = \frac{D_c}{R_{Si}} \times R_{SiO_2} \tag{3.5}$$

$$D_{SiO_2} = \frac{450um}{1um/min} \times 0.00025um/min = 0.1125um \qquad (3.6)$$

This means the minimum thickness of SiO_2 should at least 0.1125um. 0.5um SiO_2 is chosen to ensure the safety. Here 500nm LPCVD TEOS is chosen as the protecting layer.

LPCVD SiO$_2$ Si   TiN
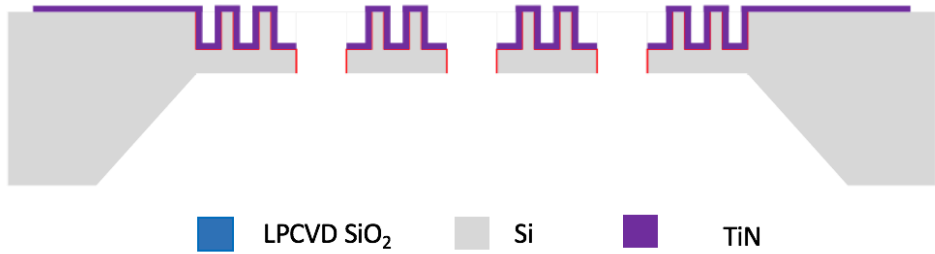
Figure 3.14

After remove all photoresister and SiO_2, Sputtering of TiN is done by Sigma. TiN thickness 500 nm. This is the working electrode of sensor.

3.3.2. Process Flowchart two

The first process flowchart has several disadvantages due to the TMAH wet etching process. More details and results will be discussed in the next chapter.To avoid the wet etching process we developed a new process flowchart and describe in the following section. The LPCVD TEOS can not protect the wafer very well. TMAH solution not only etch through the wafer but also destroy the pillar structure. Flowchart two below show improvement of flowchart one which use DRIE etching. DRIE etching is more controllable even through it take more time. Figure 3.15 show the zerolayer fabricated
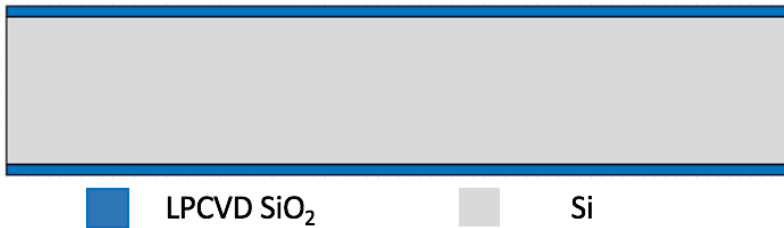
Figure 3.15

with the same method as processing one. Wafer type for processing two is 300um rather than 500um in processing one because DRIE etching is time consuming.

Figure 3.16

Figure 3.16 show that there is a light blue layer below the LPCVD SiO_2 layer. This is 3um SiO_2. This SiO_2 is deposited by "Novellus Concept 1" with recipe STDOXIDE and deposition time 48 second. PECVD (Plasma-enhanced chemical vapor deposition) is used in this step because 3um deposition by LPCVD is time consuming. Fig.3.17 below show that the deposition time for 2.98um is about 17.88 hours which is much longer than PECVD oxidation.

After testing, the result etching rates of DRIE is listed in Chapter 6. The
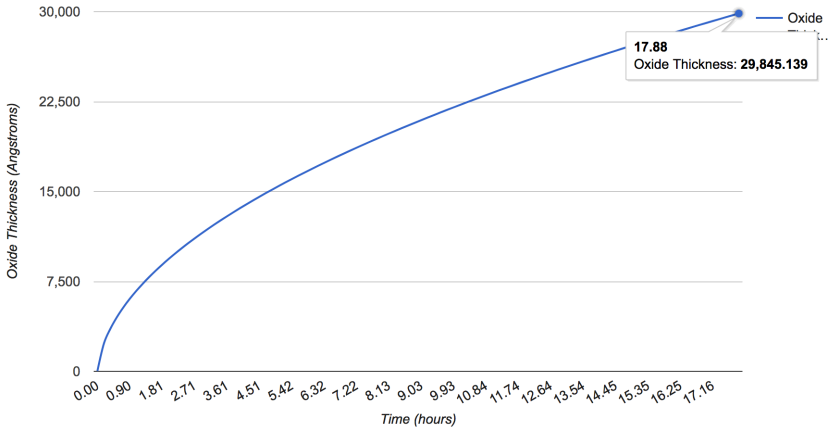
Figure 3.17: Deposition time of $3umSiO_2$ by LPCVD

maximum etching rate of SiO_2 is about 5.6$nm/cycle$ and the etching rate of Si is 1.68$um/cycle$ when using recipe "$xxEKL - smooth - xxx$". Assume 300um wafer need to be etched through under this etching rate of SiO_2. The thickness of SiO_2 need to be:

$$T_{SiO_2} = \frac{300um}{1.68um/min} \times 5.6nm/min = 1um \tag{3.7}$$

In order to ensure safety, 3um SiO_2 is deposited in this step on the backside of wafer.
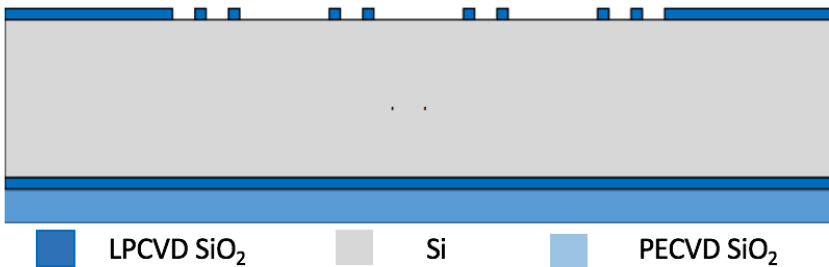
Figure 3.18

Purple layer in Fig.3.19 show the photoresister Which is the mask of etching diffusion holes. Backside SiO_2 is etched by Drytek Triode 384T with recipe STDOXDE. 10 minutes etching time is chosen due to etching rate of this recipe is 6.9nm/s. Over etch is needed because the SiO_2 must be
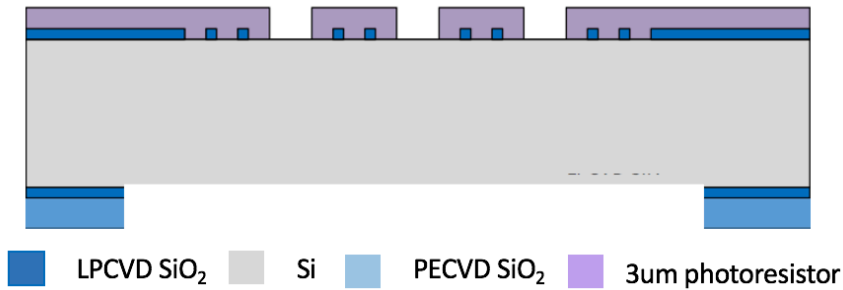
Figure 3.19

totally opened so that Si on backside can be etched. The etching time is:

$$t = \frac{3000nm + 500nm}{6.9nm/s} = 507.24s \approx 8.454min \tag{3.8}$$
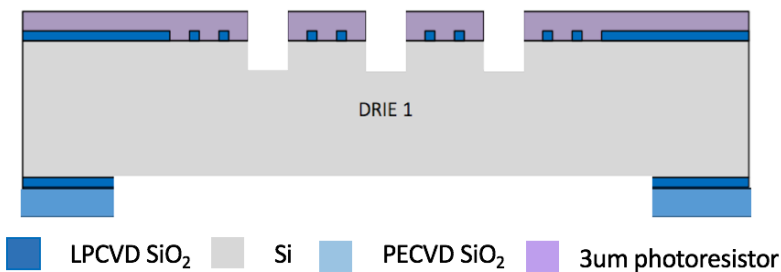
Figure 3.20

Figure 3.20 represents the DRIE etching of diffusion holes in the front side. Holes with the depth of 40um were achieved. The etching time was determined by the equation below:

$$t = \frac{T_{dif}}{R_{scribline}} = \frac{40um}{2.67um/min} = \approx 15min \tag{3.9}$$

As illustrated by figure 3.21, pillars structures were built in this step after the photoresistor (purple layer) was removed on the top of front side. Different etching recipes were tested to achieve straight and smooth pillars. Details of etching method will be discussed in the following section.

The red thin layer on the top of pillars was 500nm SiO_2 deposited by LPCVD. This SiO_2 layer was a protecting layer which protected the wafer when cavities on back side were etched.

DRIE 1

LPCVD SiO$_2$ Si   PECVD SiO$_2$

Figure 3.21

Thin thermal oxidation

LPCVD SiO$_2$ Si   LPCVD TEOS

Figure 3.22

LPCVD SiO$_2$ Si   LPCVD TEOS
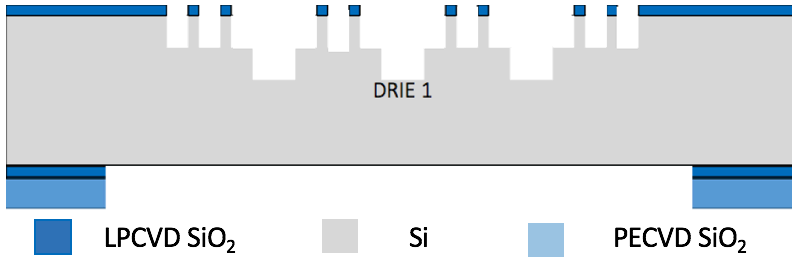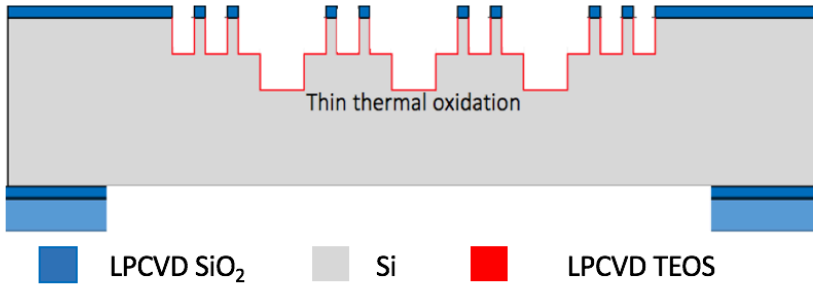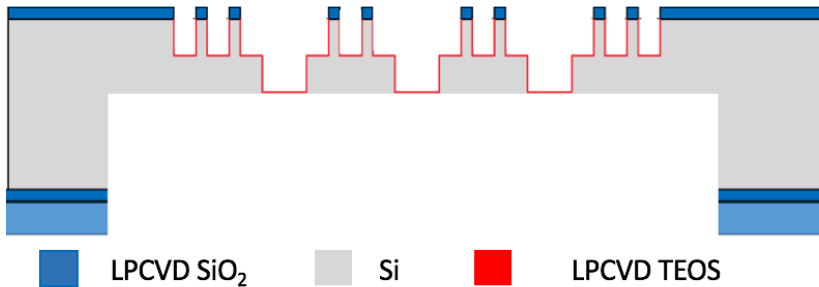
Figure 3.23

Figure 3.23 demonstrates the etching of cavity on backside of wafers. The recipe "$SCRIBLINE\square0\square temperature$" of Adixen AMS100 was used. Etching time is:

$$t = \frac{300um - T_{diff} + T_{pillars}}{R_{scribline}} = \frac{300um - 20um - 40um}{2.67um/min} \approx 89.89min \quad (3.10)$$

For this etching, approximate 89.89 minutes of etching was applied firstly. Further small depth of etching was need to ensure that every diffusion holes

were open. Because the etching rates were different between the center part of wafer and the edge of wafer. Etching time of small depth of etching is 30 second. After this small depth of etching, sample should be checked in microscope. In the case that not all the diffusion hole were opened, another small depth of etching is need with the same etching time. This two steps were repeated until all diffusion holes on wafers open. Time was controlled strictly to avoid the wafer etched through. The maximum etching time of small depth etching can be derived from the equation below:

$$t_{max} = \frac{40um}{2.67um/min} = 15min \tag{3.11}$$

As figure 3.24 show below, if etching depth exceed 40um wafers will be etched through. After removing the SiO_2 layer on the front side, there will be no pillars any more. As can be seen from Figure3.24, the sidewall of backside cavity is straight rather than a slop that got in the flowchart one after wet etching. Because DRIE etching is completely anisotropic etching and tetramethy lammonium hydroxide is partially anisotropic etching which will etch alone <111> crystalline.
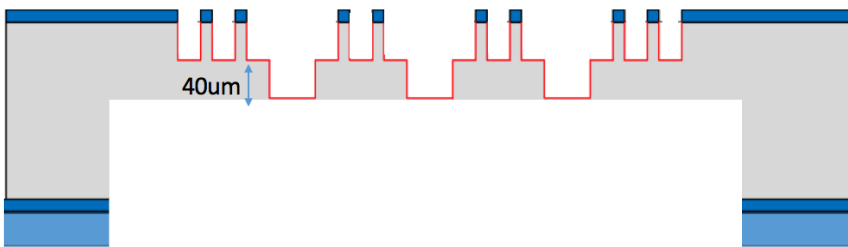
Figure 3.24: Maximum etching time of small depth of etching
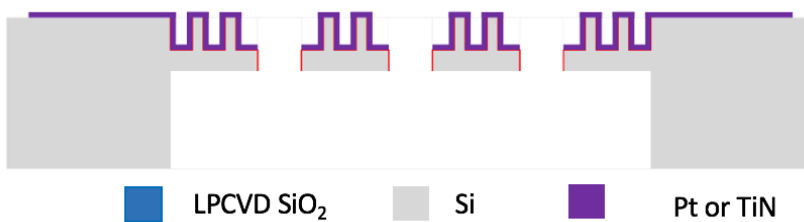
Figure 3.25

Figure 3.25 illustrate the deposition of working electrode. After etching of cavity on backside, all SiO_2 was removed by $BHF1:7$. The etching rate of etching SiO_2 in $BHF1:7$ is $70nm/min$. The maximum SiO_2 thickness was

3500nm on the backside of the wafer. Thus, the minimum etching time for removing all SiO_2 is:

$$t = \frac{T_{SiO_2}}{r_{BHF}} = \frac{3500nm}{70nm/min} \approx 50min \tag{3.12}$$

Before the deposition of TiN as working electrode, LPCVD TEOS were deposited on the top of pillar. This SiO_2 layer serve as a adhesion layer for TiN. Then, 500nm TiN is sputtered on the top of wafer on the front side by "Trikon Sigma". Standard lift-off process were applied that the expected electrode pattern can be got.

3.3.3. Process Flowchart three

The third flowchart was designed based on screen printed electrode. This was because print-electrode of Dropsens including sensor, connector and wire was made by platinum. This way can eliminate the possible effect factor that other metal can interfere with working of platinum working electrode.
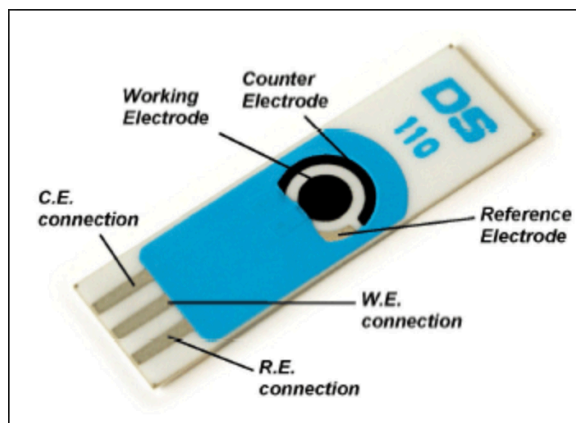
Figure 3.26: Printed platinum electrode designed by Dropsens

As compared with 3D electrode processed by second flowchart, Printed electrode designed by Dropsens show very good measurement result in voltammetric measurement as shown in Figure 3.27.

Cyclic voltammograms of $1 \cdot 10^{-4}$ M $K_3[Fe(CN)_6]$ in 0.1 M KCl electrolyte solution at a scan rate of 50 mV/s. n = 5 (ref. 550)
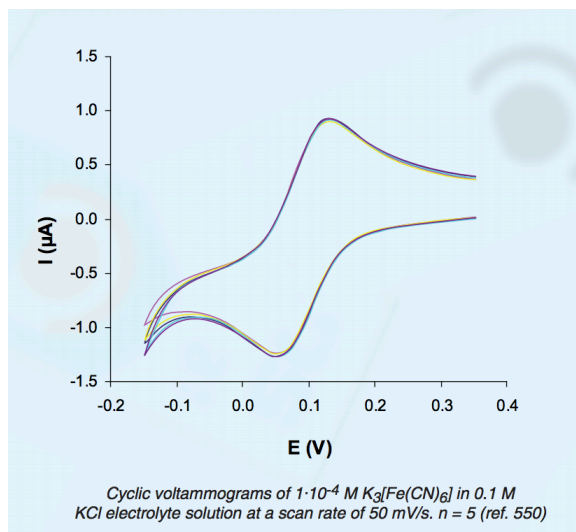
Figure 3.27: Cyclic voltammetric measurement of printed platinum electrode

3

The aim of third process was making 3D sensor with pillars and diffusion holes and using the same packaging method with Dropsens. This packaging method required no wire bonding, no connector and no any glue. All of these parts were made in wafer level and were covered. By this way, the only signal was the one that coming out from platinum working electrode. The general dimensions of printed electrode was $3.4x1.0x0.05cm$. This size already had exceeded the maximum size that of stepper mask($3mm*3mm$) for each die. Therefore, file masks to be used in contact aligner were designed.

Shadow Mask

Shadow mask was used as mask of whole structure. In previous flowcharts, last step was done by lift-off to remove residual platinum. It also could be done in flowchart three but it was time consuming and has difficulty due to long process with lift-off procedures. As shown in Figure 3.28 , Si wafer with hollow pattern was served as a shadow mask when doing evaporation. The advantage of this why was avoiding complicated lift-off of platinum and only thing need to do was sticking shadow mask on the top of front side of sample wafer. So that only hollow pattern parts will be covered with platinum for sample. Figure below show the how the shadow mask work
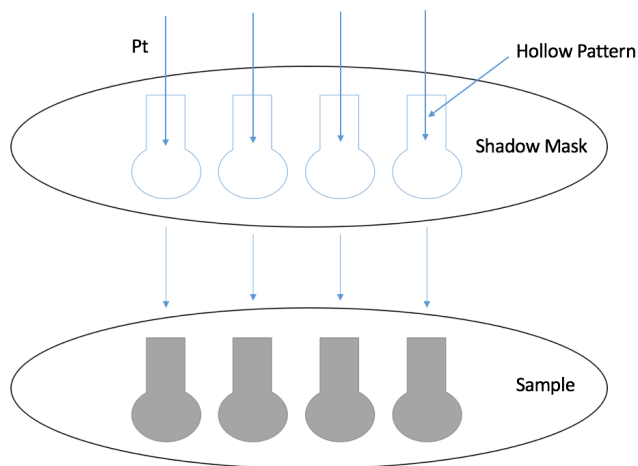
Figure 3.28: Working function of Shadow mask

As shown in figure3.28 Pt molecular will passed through the hollow pattern of shadow mask and reached the sample that need to be deposited.

Flowchart Three

SI WAFER : WITH ZERO LAYER
ZEFWAM on front side

Figure 3.29

3
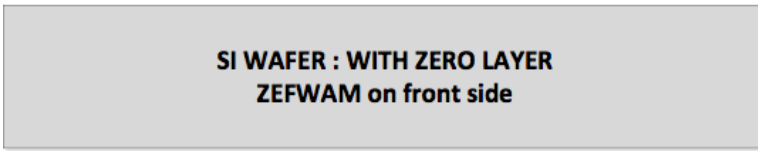
For the zerolayer of flowchart three, recipe ZEFWAM of "ASML PAS 5500/80 waferstepper" was used instead of "comurk0.0" which was used in the flowchart one and flowchart two. Because the exposure for pillars and diffusion holes would be done in "EVG 420 Contact Aligner" with file mask. And the recipe of backside aliment mark was "FWAMtoftbaze" which means making an aliment mark on the backside on the same place that aliment mark on the front was. Other steps of Zerolayer were the same with previous flowchart. 3um PECVD SiO_2 were deposited on both front side and

LPCVD SiO$_2$ Si
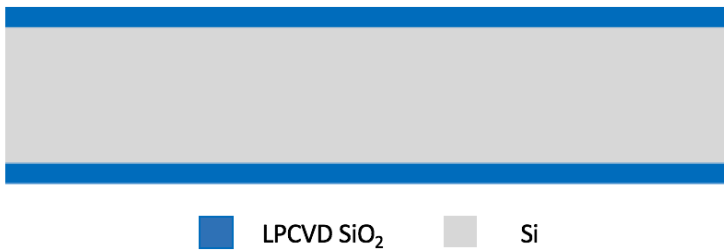
Figure 3.30

backside. Because in this flowchart, there was no backside cavity. Diffusion holes were etched through backside directly. And all exposure for

LPCVD SiO$_2$ Si
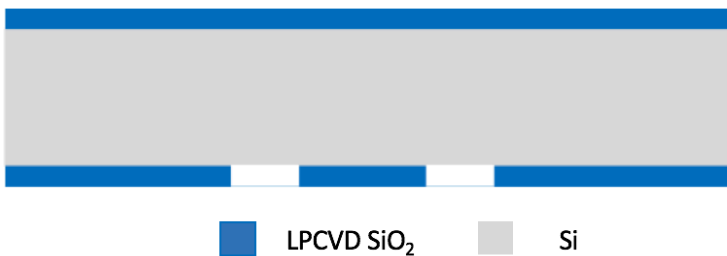
Figure 3.31

hard mask were made by "EVG 420 Contact Aligner" with exposure time 30 second. Front to Front exposure was chosen because front of mask

LPCVD SiO$_2$ Si

Figure 3.32

3
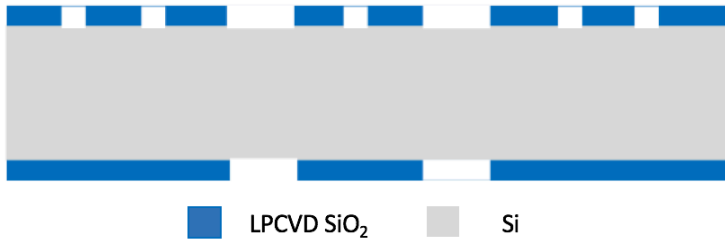
attached to the front of wafer that need to be exposed The larger scale of pillars, diffusion holes and electrode were designed due to minimum size limitation of file mask. Therefore, the pillars height can be higher than the pillars in previous flowcharts. And because the distance of pillars became larger, another machine "Trikon Omega 201" was tested to etch the pillar structures with recipe "Deep-Si". The etching time is set to 30 minutes. Details of limitation of height of pillars will be discussed in later section.
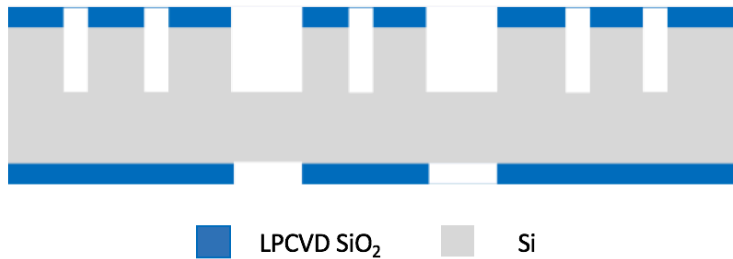
LPCVD SiO$_2$ Si

Figure 3.33

Before etching diffusion holes, 500nm LPCVD SiO_2 were deposited on the front side of pillars. This thin film of SiO_2 served as a landing layer when diffusion holes on backside were etched. The etching time for diffusion holes should be calculated depending on the height of pillars with the equation 3.13.

$$t_{diffusionhole} = \frac{T_{wafer} - T_{pillars}}{R_{Si}}$$ (3.13)

All SiO_2 should be removed by BHF(1:7) around 30 minutes. All cleaning steps which used "Tepla Plasma 300" after DRIE etching should be done with "recipe 20" to ensure the wafer was clean enough. 3um LPCVD SiO_2 was deposited and removed again with BHF(1:7) because there were many scalloping on the sidewall of wafers after DRIE etching. Then 500nm $SiO_@$ was deposited on the front side to increase the adhesion of Platinum.

LPCVD SiO$_2$ Si

Figure 3.34

LPCVD SiO$_2$ Si   500nm SiO2

Figure 3.35

SI WAFER

Figure 3.36

SI WAFER

LPCVD SiO$_2$ Si   Pt
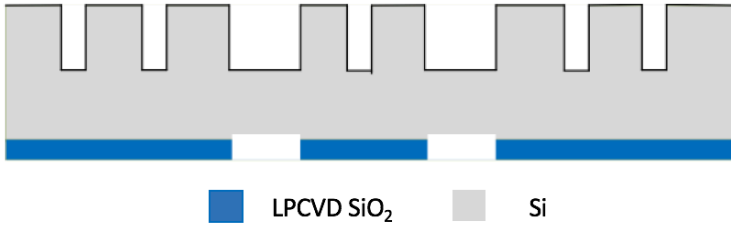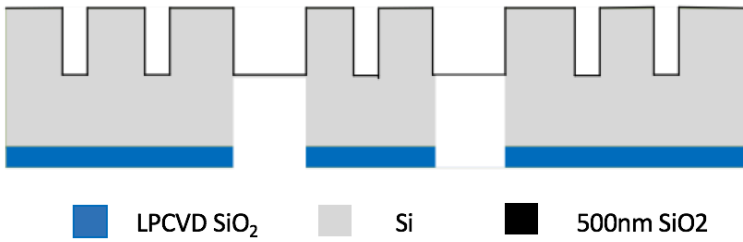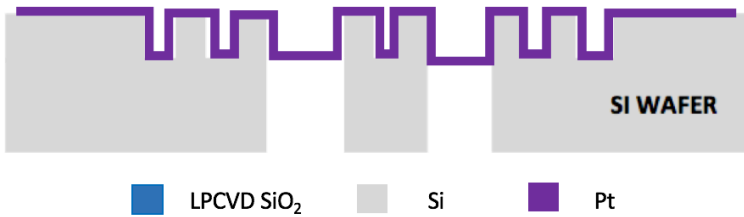
Figure 3.37

For the evaporation, same method were used. Three times evaporation were done for sidewall of pillars with tilting tool and one time evaporation was done for bottom plain. For each time, Tantalum were deposited before each time of evaporation as adhesion layers.

4

Processing Challenges and Results

4.1. Process Challenge and Result of Flowchart one

4.1.1. DRIE Etching Rate Test

Etching rates are very important parameters in all run of process. This section list all relative etching rates. 500um n-type test wafers are used. Wet etching solution is TMAH. "Adixen AMS100" and "Rapier Omega i2L etcher" is the machines for DRIE etching. Another test etching is done in Trikon Omega 201. This is no bosch etching and the recipe is Deep-Si. The test results are listed below.

4.1.2. Profile Angle of Pillars

One concept "micro-pillar profile angle" is introduced here when method of etching straight pillars are discussed. The micro-pillar profile angle refer to the angle between the top surface and the sidewall of the micro-pillar.

Figure 4.1 a demonstrates a typical micro-pillar profiles whose profile angles is larger than 90^0. Figure 4.1 b shows a micro-pillar profiles with profile angles smaller than 90^0. A pillar with nearly 90^0 profile angle is illustrated in 4.1 c. Different profile angle of pillars caused by different DRIE process conditions. Theoretically, as figure 4.1 a shows, the profile

	Rapier Omega i2L	
	xxEKL smoothxxx	AJ_Mapper_Speed
Si	1.68um/cycle	0.652um/cycle
SiO2	5.6nm/cycle	4.3nm/circle

Table 4.1: Table of etching rate of Rapier Omega i2L

	Trikon Omega 201	TMAH	Adixen AMS100
	Deep-Si		scribline
Si	1.33um/min	1um/min	2.67um/min
SiO2	15nm/min	0.25nm/min	5.9nm/min

Table 4.2: Table of etching rate of other machine

(a)   (b)   (c)
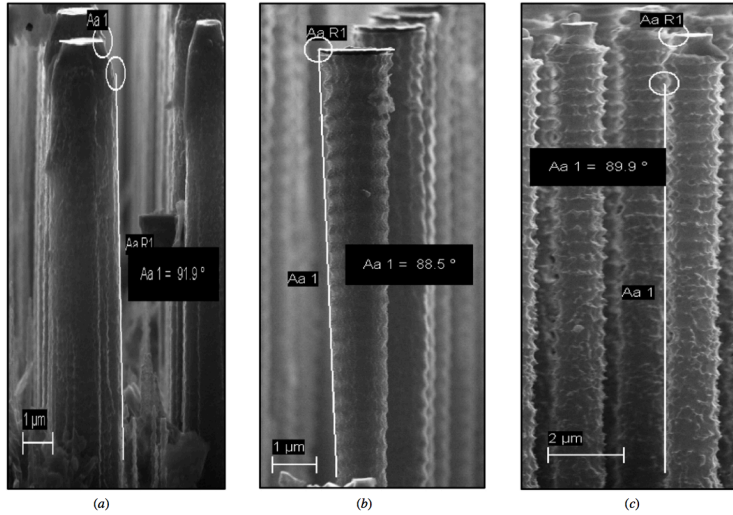
Figure 4.1: Different types of profile angles of pillar structures.[11]

angle of the pillars will increase (i.e. the pillars will be wider at the bottom than at the top or the profile angle will become more positive) when the etch cycle time decreases while the passivation cycle time increases. In this situation, a profile angle will be larger than 90◦ On the other hand as figure4.1 b shows, the profile angle of the pillars will decrease when the the passivation cycle time decreases or etching cycle time increases. Because both ways will lead to over etching. In this case, a profile angle smaller than 90◦ Vertical micro-pillars in figure 4.1 (c) are obtained along the 90◦ Besides the time of etch and passivation, platen power is another parameter that effect the profile angle.

For the step of etching pillars, straight pillars or pillars of positive profile angle were expected. Because these kind of pillars were more suitable for deposition of platinum. As shown in figure4.2, red region will not cover with platinum because the edge of pillar in the middle block the bunch of platinum. Compared to negative profile angle, the pillars with 90^0 profile angles and the positive profile angles can have better coverage of platinum as the figure4.3 and the figure4.4 show below.

In this etching step, different recipes were tested. Among them, "scre-beline", "AJ-Mapper-speed" and "xxEKL-smoothXXX" were reliable recipes
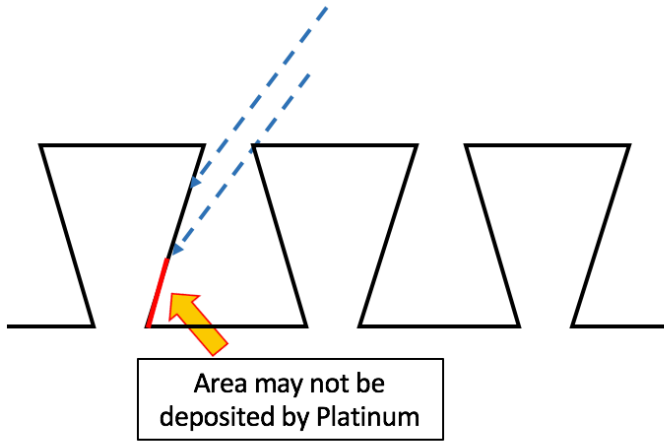
Figure 4.2: Evaporation of pillars with negative profile angle
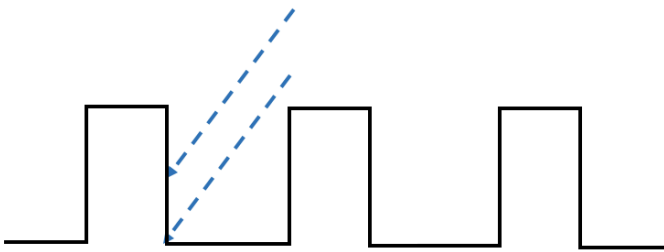
Figure 4.3: Evaporation of pillars with 90^0 profile angle
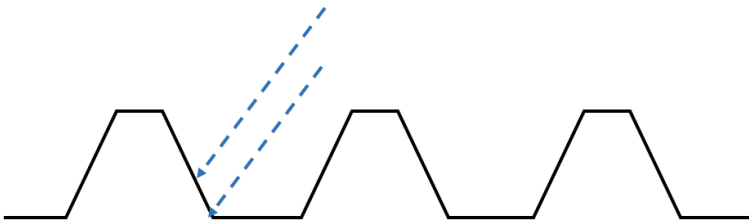
Figure 4.4: Evaporation of pillars with positive profile angle

which can achieved straight pillars or positive profile angle.

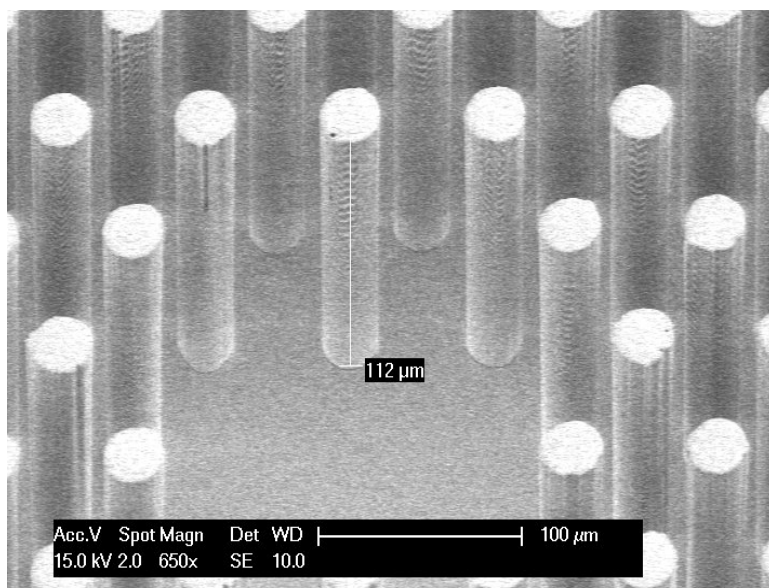As can be seem from SEM photos above, pillars that was etched by AJ-

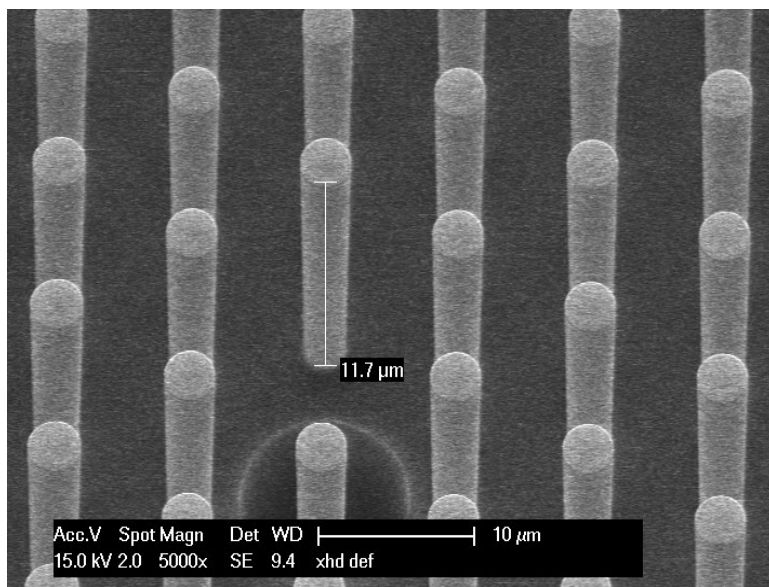Figure 4.5: SEM photo of pillar structure which is etched by recipe A□Mapper□Speed of Rapier Omega i2L

Figure 4.6: SEM photo of pillar structure which is etched by recipe scribline of Adixen AMS100

Mapper-Speed is really straight. The height of pillars were:

$$h_1 = h_{AJ-Mapper-Speed} \times 2 = 224um \tag{4.1}$$
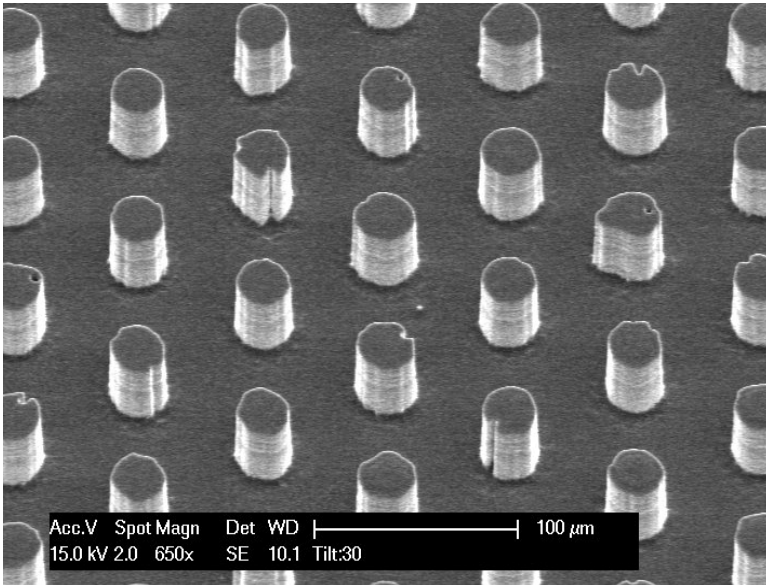
Figure 4.7: SEM photo of pillar structure which is etched by recipe xx-ekl-smooth-xxx of Rapier Omega i2L

Pillars that were etched by "Scribline" had negative profile angle but they were very close to 90°. And the the profile angle of Pillars that were etched by recipe "xxEKL-smoothxxx" were positive.

As figure4.8 illustrates, the profile angle can be calculated by equation below:

$$\tan \alpha - 90^o = \frac{h}{\frac{a_1 - a_2}{2}} \tag{4.2}$$

Where h is the height of pillars, a_1 is the diameter of the top surface of pillars and a_2 is the diameter of the bottom surface of pillars.

$$\alpha = \tanh \frac{h}{\frac{a_1 - a_2}{2}} + 90^o \tag{4.3}$$

For the figure 4.8, the tilting angle of wafer was 30 degree. The height of pillars can be derived from the figure 4.9 below. Thus, the height of pillars is:

$$h = (90^o - \beta) \times h_{SEM} \tag{4.4}$$

Where β is the tilting degree. All these sample were inspected under the tilting degree of 30° in SEM. Therefore, according to figure 4.9 the height of pillars etched by recipe "xx-eklsmooth-xxx" were:

$$h = 2 \times 22.1um = 44.2um \tag{4.5}$$
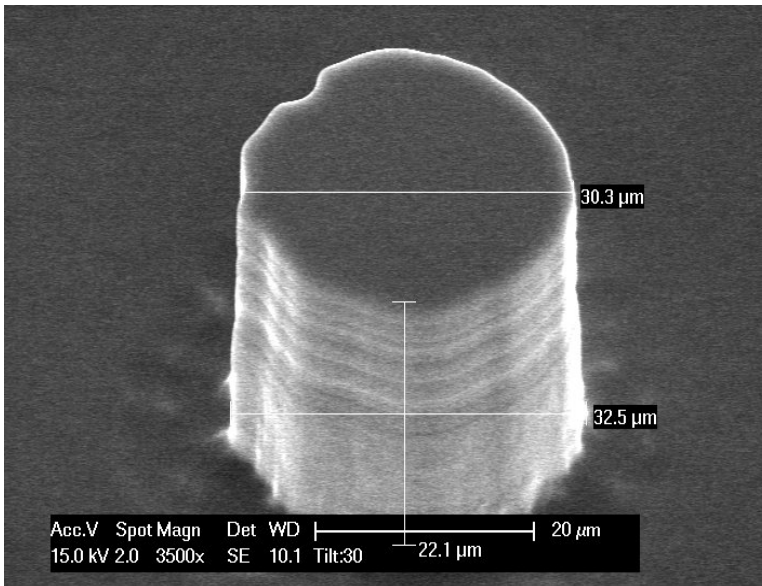
Figure 4.8: Profile angle of pillars that were etched by recipe "xx-EKLsmooth-xxx"

Thus the profile angle of pillars that were etched by recipe $"xx-eklsmooth-xxx"$ is:

$$\alpha = 90 - \tanh \frac{44.2}{\frac{32.5-30.3}{2}} + 90 = 91,42^o \tag{4.6}$$

Figure 4.10 shows one of negative profile angle that etched by other recipe.

4.1.3. Surface Defect of Pillars

Besides profile angle of pillars, surface defect is another problem of DRIE etching. Temperature is the most essential parameter that relate to surface defect. When temperature is low, passivation layer will become thicker. Thicker passivation layer can have a better protection of surface of pillars. In contrast, higher temperature will lead to thinner passivation layer, so that more defects are on the sidewall of pillars after DRIE etching.

Figure 4.12 shows the etching result of recipe "scribline" under temperature $10^o C$. There were defects on every corner of the top surface of pillars. There are two possible reasons for this phenomenon. Firstly, the passivation layer is not thick enough due to high temperature. It can not protect top edge of pillars. Basically, when the DRIE etching goes deep into silicon, the power will increase so that to ensure that ions can etch deeper into silicon. However, the passivation layer that deposited in the first cycle of etching will be consumed with time. When the etching power increase to a certain point, passivation that deposited in first cycle is not enough to
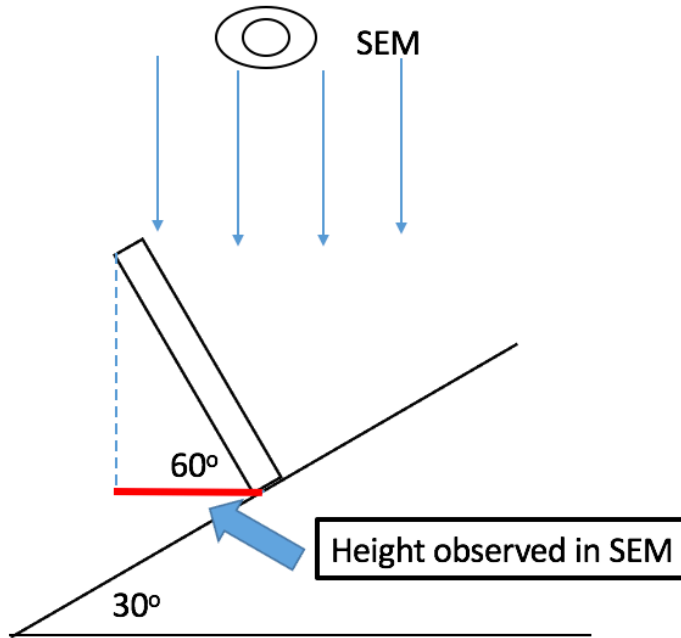
Figure 4.9: Calculation of height of pillars through SEM photos

protect the sidewall anymore. The sidewall of this part will be etched.

From the stress simulation below, another possible reason why defects occur on the top corner can be got.

As the figure4.13 a shows, this model only concerns the stress distribution when the ion bombard sidewall of pillars. In order to simplify the model, the force that ion provide is equally distributed on the sidewall of pillars. Basically the most ions hit the sidewall because of the reflection of bottom plane. In this simulation, different angle of ions direction were tested with the same total force. Figure 4.13 b show the boundary conditions of this model built for comsol. Bottom of pillars were set to fix constraint. Because the selectivity of Si to SiO_2 was very high. As equation below shows the selectivity of Si to SiO_2 of recipe "scribline"

$$Selectivity = \frac{R_{si}}{R_{SiO_2}} = \frac{2.67um/min}{5.9nm/min} \approx 452.54 \tag{4.7}$$

This means there will be nearly no damage of SiO_2 mask when the Si bombard the structure. $\sqrt{2}N/m^2$ forces were applied to sidewall. This force will have different component vectors when the ions change injecting direction. Different injecting angles have been simulated as the table4.3 shows.

As can be seen from figure**??**, when the refection angle of ions become larger, the strength that the corner of top surface of pillars suffer become
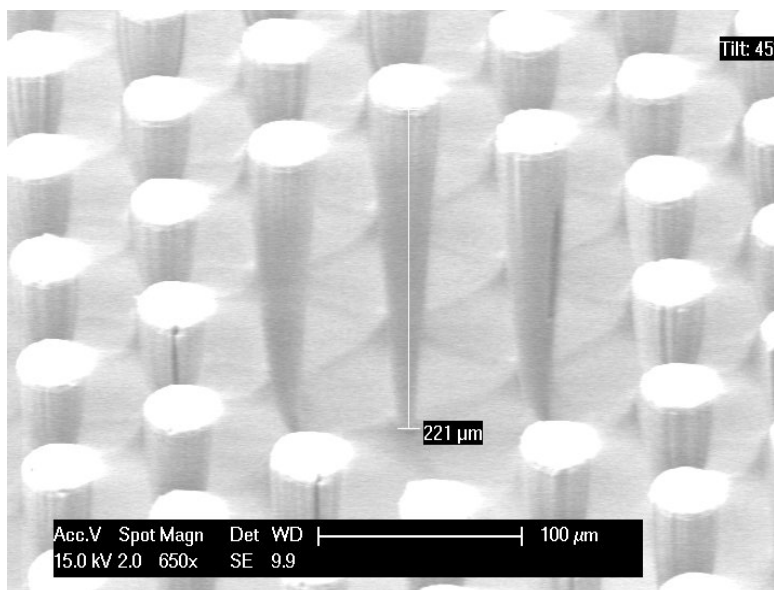
Figure 4.10: Pillars with negative profile angle
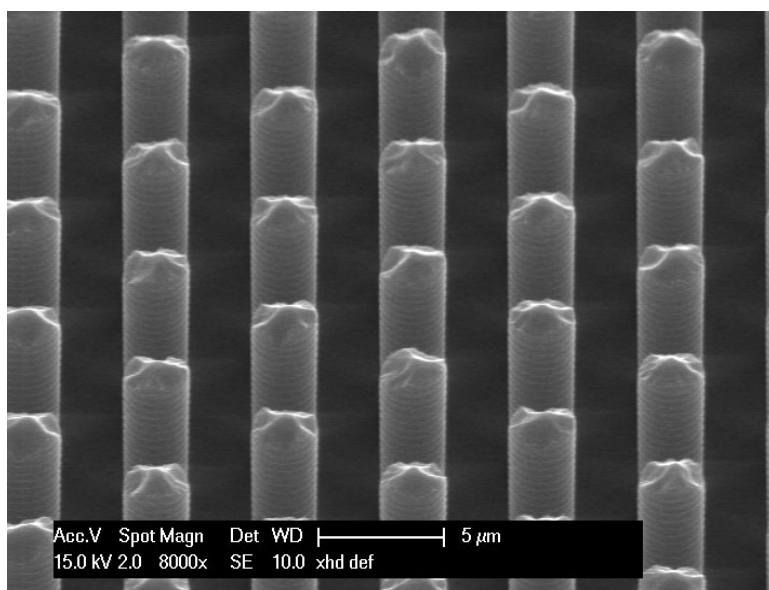
Figure 4.11: Defect of surface of pillars

larger. For the whole system, the strength that top corner suffer is:

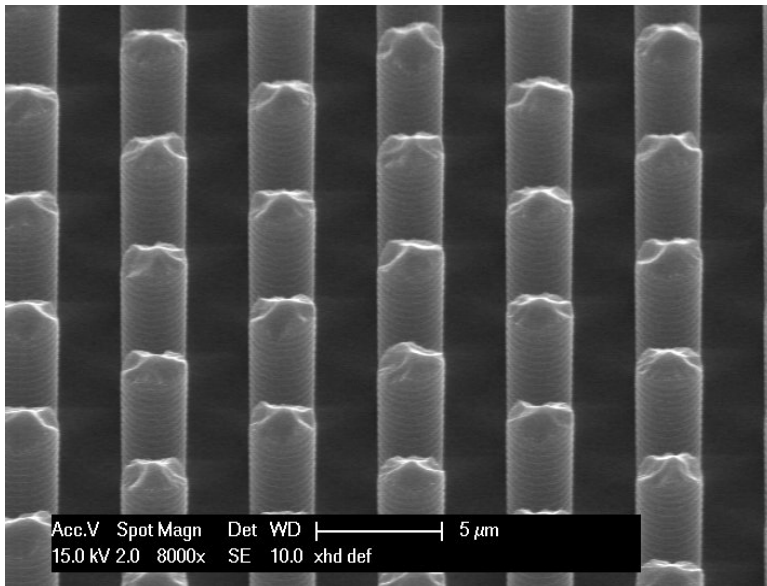$$F = \sum_{n=1}^{\infty} F_n (n = 1, 2, 3......) \tag{4.8}$$

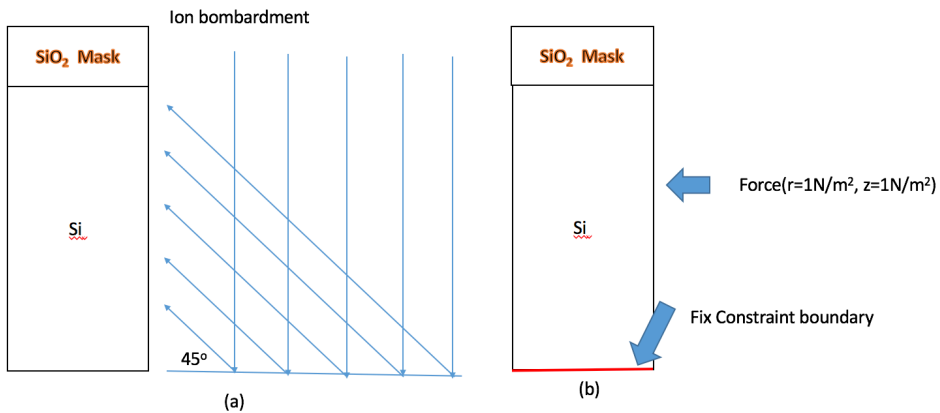Figure 4.12: Defect of surface of pillars

Figure 4.13: Model building of stress distribution of pillars structure

The simulation result shows, the top corners of pillars will suffer the maximum strength or have the largest displacement for every F_n when they are compared with other part of pillars. Therefore, the corners of top surface of pillars will suffer maximum force when all ions bombardment effect are added together. Therefore, nearly all of the edge of pillars have such kinds of defects after etching.

In order to solve this problem, lower temperature was set. From experi-

	r	z	degree
1	1.366	0.366	15°
2	$\sqrt{6}/2$	$\sqrt{2}/2$	30°
3	1	1	45°
4	$\sqrt{2}/2$	$\sqrt{6}/2$	60°

Table 4.3: Simulation parameter about the component vectors along r and z direction of the force that ions supply to sidewall of pillars
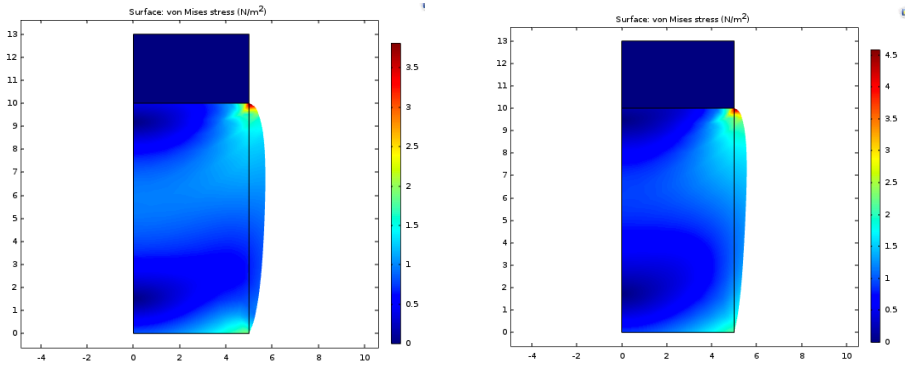
Figure 4.14: Result of stress distribution of pillar structure when ions bombard the sidewall of pillars with degree of (a), (b)15°, (c)30°

ence, lower temperature of platen will increase the thickness of passivation layer. So that it can bear more bombardment energy. what is more, typical kinetic energy (KE) of an electron in plasma is:

$$Ke = \frac{1}{2}mV^2 = \frac{3}{2}KT \qquad (4.9)$$

Thus ions will have less destructive under lower environment temperature. What is more, temperature controlling device in Rapier is the platen. When the ion crash to the cooled platen, there is energy exchange between ions and platen. The lower is platen temperature is , the more energy will be exchanged between ions and platen. Thus the kinetic energy of ions will be reduced.

Figure 4.16 shows the result of pillar structures that were etched under temperature 0°. There was no defects on the edge of top surface anymore. However, too much lower temperature was also not good for etching of pillars.

As figure4.17 show, along the edge of diffusion hole, there was still silicon that was etched. This is because the passivation layer is too thick that the edge of diffusion holes can not be etched. From all the results above, conclusion can be made that 0 degree is most suitable temperature to get straight pillar without defects.
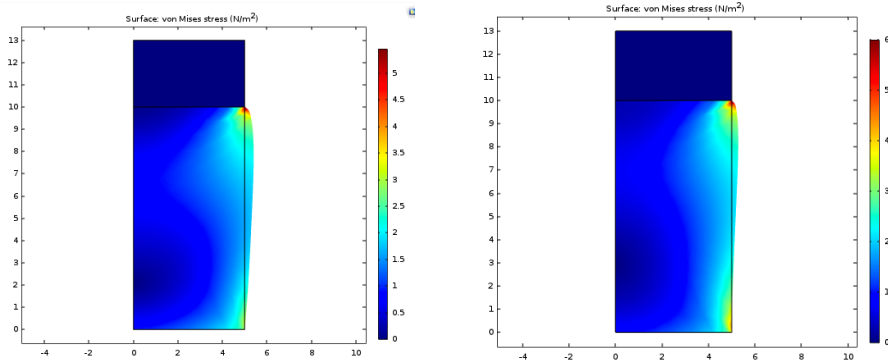
Figure 4.15: Result of stress distribution of pillar structure when ions bombard the sidewall of pillars with degree of (a), (b)15°, (c)30°
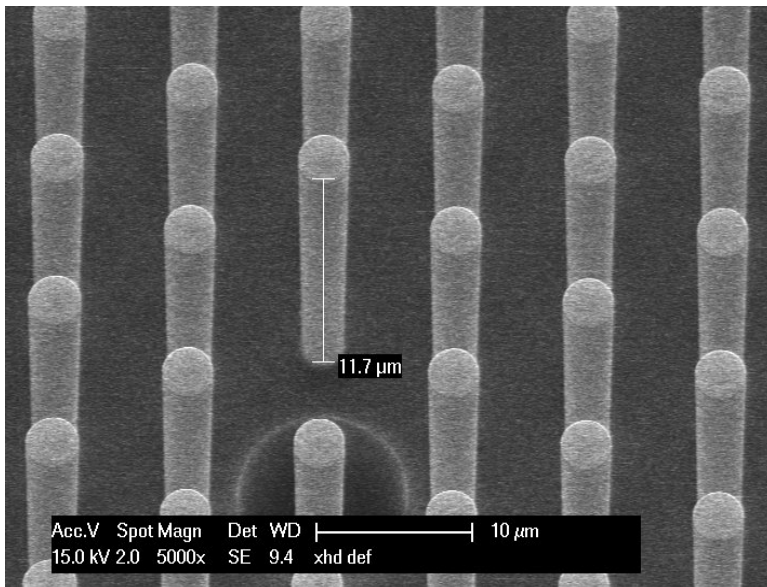
4

Figure 4.16: Pillars structure after DRIE etching with recipe"scribline" in 0 degree

4.1.4. Processing Result of Flowchart one

Figure 4.18 show the result of the processing of flowchart 1

As can be seen from the figure, most dies of this sample has been destroyed. These dies have been etched through, hence, there is no pillars any more. This problem occur after wet etching of backside cavity. Theoretically, pillars can be protected well. As mentioned in previous chapter. As show in Fig.4.19 below, the time that wet etching take is:

$$t = \frac{T_c}{R_{Si}} = \frac{450um}{1um/min} = 450min \tag{4.10}$$
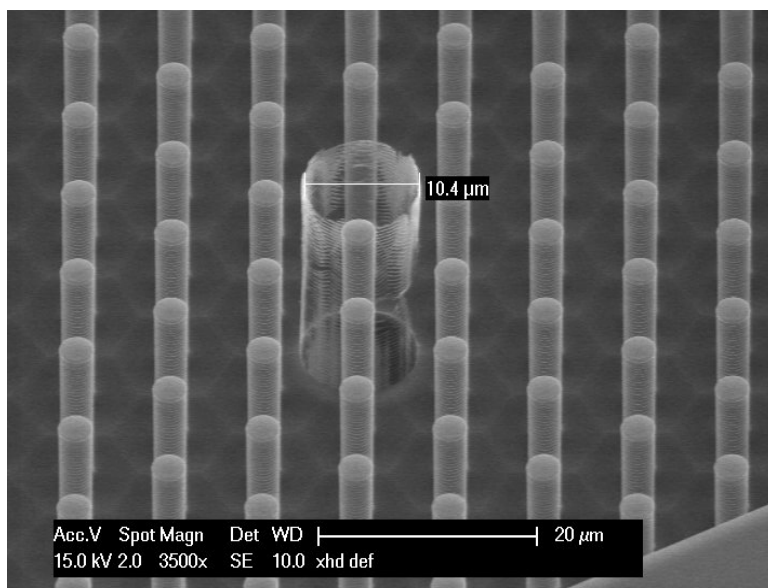
Figure 4.17: Result of pillar structures after DRIE etching with -10° temperature
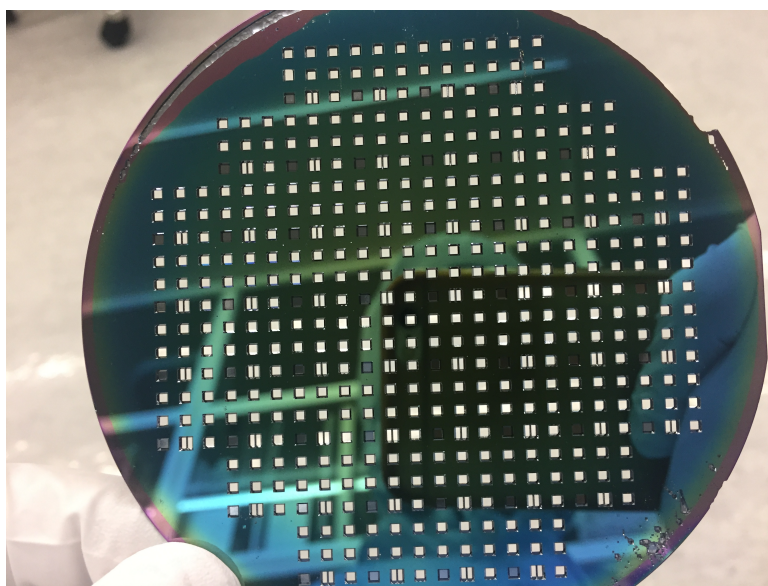
Figure 4.18: Result of sample of after wet etching

During this period, the thickness of the front side SiO_2 that have been etched is:

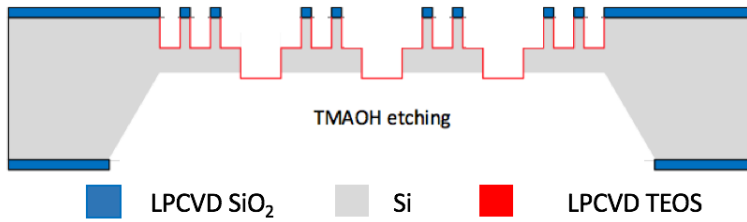$$T_{SiO_2} = t \times R_{SiO_2} = 450min \times 0.25nm/min = 112.5nm << 500nm \qquad (4.11)$$

TMAOH etching

LPCVD SiO$_2$ Si   LPCVD TEOS

Figure 4.19: Wet Etching of backside cavity in flowchart 1

$$r = \frac{R_{SiO_2}}{R_S i} = \frac{0.00025um}{1um} = 0.00025 \tag{4.12}$$

As show in equation4.12 above, the etching rate of SiO_2 is much lower com-
pared to that of Si. The theoretical residual thickness of SiO_2 is

$$T_r = 500nm - 112.5nm = 387.5nm \tag{4.13}$$

Therefore, the possibility of etching through the wafer from front side is
very low. Basically, there could be two reasons that cause the damaging
of wafer. One is the density of SiO_2 deposited by LPCVD TEOS is not good.
Thus, TMAH penetrate through the SiO_2 and destroy the whole structure.
Another reason is the real etching rate of Si from backside is quicker than
theoretical value so the wafer is etched through from backside. However,
over etch is needed because diffusion hole need to be opened. Practically,
the solution for these two issues need further investigation.

4.2. Measurement Result of Flowchart two

4.2.1. Cyclic Voltammetric Study

Cyclic voltammetry (CV) is a versatile electroanalytical technique for the study of electro- active species. CV monitors redox behavior of chemical species within a wide potential range. The current at the working electrode is monitored as a triangular excitation potential is applied to the electrode. The resulting voltammogram can be analyzed for fundamental information regarding the redox reaction. Cyclic voltammograms are the electrochemical equivalent to the spectra in optical spectroscopy.

4.2.2. Measurement of TiN
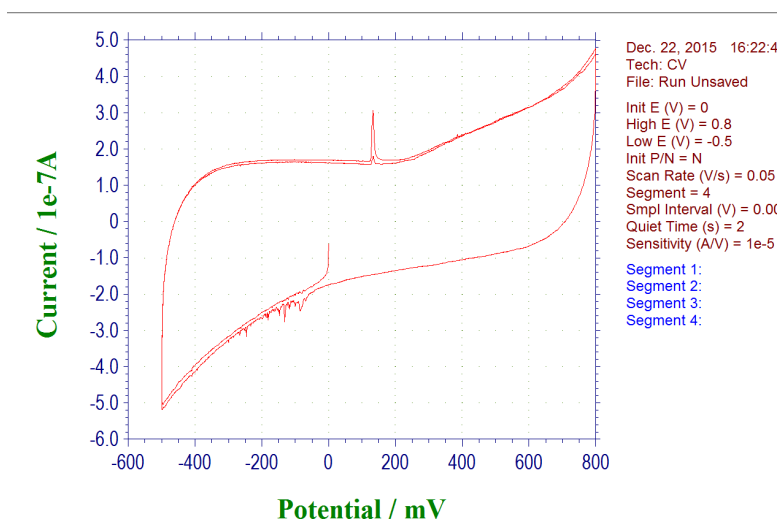
Figure 4.20: Cyclic Voltammogram of TiN

For the second flowchart. There was no problem of processing. Every step was fine and perfect sensor structure had been got with TiN working electrode sputtered on the sensor surface.

However, as the figure 4.20 shows, the peak of oxidation and the peak of reduction can not be seen when it was compared to the standard cyclic voltammogram as showed in fig4.21. There is nearly no redox reaction happen when TiN is used as a working electrode. The current of TiN ranged from 0.1uA to 0.5uA which is much smaller than theoretical value around 10uA. The cyclic voltammetric measurement of TiN only show the capacitive behavior which was only charging and discharging behavior of applied excitation signal through auxiliary electrode.

In conclusion, from the measurement result above, TiN was not good metal that could be used for electrochemical sensor. Because aims of electrochemical sensor was to detect the amount of redox products by measur-
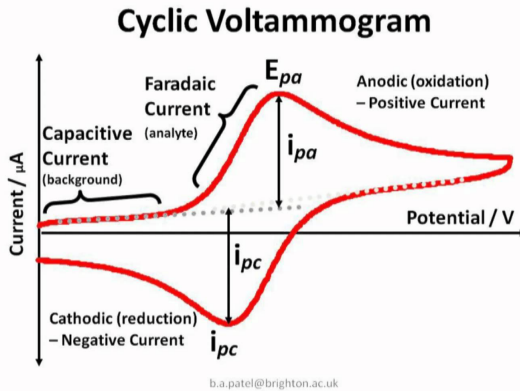
Figure 4.21: Example of Standard Cyclic Voltammogram

ing the amount of electron that were captured from redox reaction.

After this run of processing, more research works had been done and many essays showed that platinum could be a good material for electro-chemical sensor[12]. Thus screen printed platinum electrodes produced by Dropsens were tested. The result of Cyclic voltammetry was shown in figure4.22 below.
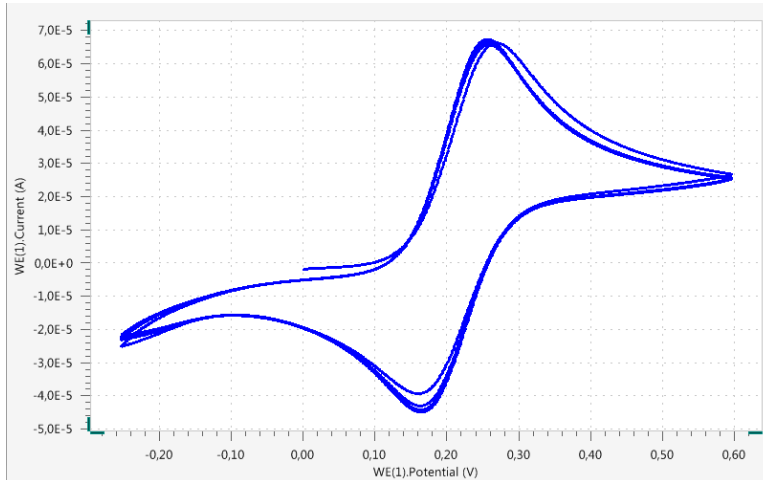

Figure 4.22: Cyclic voltammetric measurement of Printed-electrode

As the figure4.22 showed, platinum has really good C-V characters be-cause clear peaks of oxidation and reduction were showed in Cyclic Voltam-mogram and the gap between the peak of oxidation and reduction was large which means this material had obvious redox behavior in the test solution.

It is good character for electrochemical sensor especially when the sensor is use inside human body. Because the signal that can be got from redox reaction inside human body is very small. The main aim of 3D electrode is to capture more electron which is the current signal that produced by redox reaction.

4.2.3. Adhesion Test for Platinum

Same processing was done only the electrode was changed from TiN to Platinum. However, platinum could not sputtered by "Trikon Sigma" as the sputtering of TiN electrode Because it is contaminated metal and is very expensive material. Only way that could be achieved in EKL is "CHA Solution Std Evaporator".

Evaporation	Sputtering
Low energy atoms (~ 0.1 eV)	High energy atoms / ions (1 – 10 eV) • denser film • smaller grain size • better adhesion
High Vacuum • directional, good for lift-off • lower impurity	Low Vacuum • poor directionality, better step coverage • gas atom implanted in the film
Point Source • poor uniformity	Parallel Plate Source • better uniformity
Component Evaporate at Different Rate • poor stoichiometry	All Component Sputtered with Similar Rate • maintain stoichiometry

Figure 4.23: Comparison of Evaporator and Sputter

Figure 4.23 shows the difference between Evaporation and sputtering and illustrates that the coverage of metal deposited evaporation is not good. When evaporator was used, good coverage of metal become a big challenge. There are three reasons that sputter can achieve better coverage. Basically, sputter create a gaseous plasma and accelerate the ions from this plasma into the target source material(TiN in process two) as the orange bar shown in figure 4.24. The target source is eroded by the arriving ions via energy transfer and ejected down to the wafer that is need to be deposited. During the period that target metal goes down to the wafer, there are multiple collisions of the metal atoms in the path between the cathode and anode. The metal atoms will arrive at the anode at random incident angles. This is the main reason why sputter can achieve better step coverage as compared with evaporation. As figure 4.24 and figure?? illustrates, as the sputtering target source is much more broader as compared with an evaporation point source, evidence of shadowing decreases drastically. Furthermore, the metal ions in sputter have higher energy due to low pressure. This will
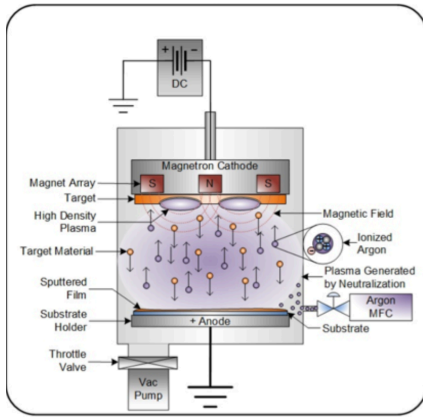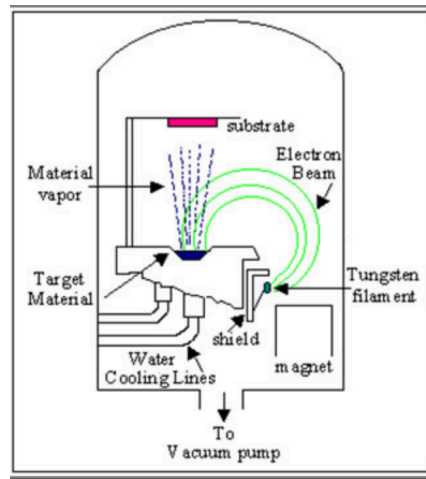
Figure 4.24: Sputter

Figure 4.25: Evaporation

leads to improved film adhesion. Thus adhesion test was done and tilting tool was designed to ensure the metal coverage of sensor

Because Platinum electrode need to be evaporated 4 times from different angles, formation of adhesion layers also require 4 times evaporation so as to ensure that the whole electrode can be coated on the adhesion layer. Due to efficiency and uniformity considerations, less steps in evaporation of platinum is expecting. Therefore, new method for depositing adhesion layers should be found. The most convenient way is evaporate platinum on oxide layer directly. In this experiment, we compare adhesion of platinum on 4 different oxide layer which consists of SiO_2, SiC, Si_3N_4 and TEOs. Experiment parameters are shown in the table below

Thickness of Oxide Layer	100nm
Thickness of Platinum	300nm

adhesive property	
SiO_2	not good
SiC	not good
Si_3N_4	not good
$TEOS$	not good

After depositing the oxide layer on wafer, we use tape to do the adhesion test. As we can see from the photo, platinum is falling when the tape is peeled off from the center to edge of wafers. The result show the adhesion of platinum is not good for all materials especially on the margin of wafers. Among these 4 oxide layers, adhesion strength of TEOS is a little bit better

4
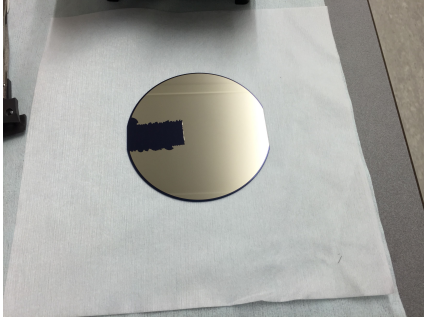
SiO_2

SIC

Si_3N_4

TEOS

than others because the beginning of falling off of platinum is closer to the edge of wafer when the start point of this test is in the center of the wafer. However, TEOS is still not the expected material because all the platinum is falling off when the start point of test change to the edge. The same result occur on other 3 oxide layer which means evaporating platinum on oxide layer directly is not feasible. In conclusion, for all of four times evaporation, adhesion layer were necessary for each times.

4

4.2.4. Evaporation of Platinum as Working Electrode
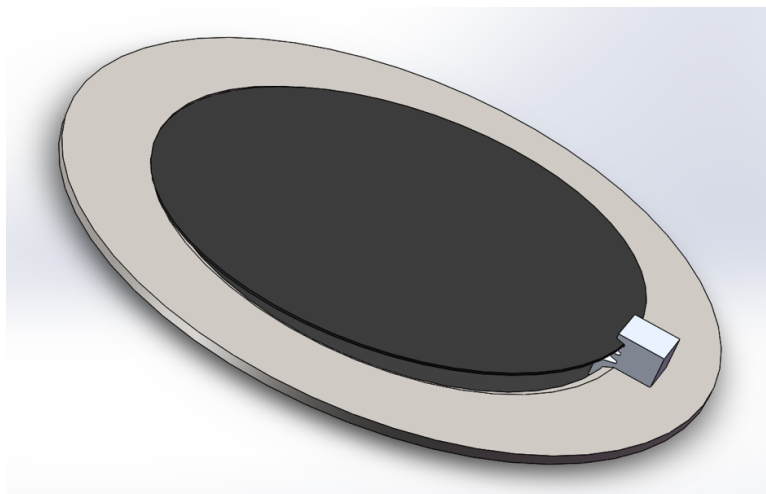
Figure 4.26: Clamp that help to tilt the angle of evaporation

In chapter two, minimum thickness of working electrode has been calculated, another challenge of process relate to working electrode are discussed here. As mentioned in previous section, evaporator can only evaporate the platinum from a point source. As shown in Fig.4.27, the sidewall of the pillars will not be covered by metal if only front side evaporation was done. Therefore a tool to tilt the angle of the wafer should be made.
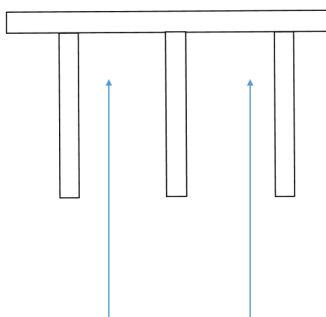
Figure 4.27: Point source evaporation who share the drawback of unable to cover the sidewall of pillar structure

Figure 4.28 demonstrates the top view of the holder of "CHA Solution STD". The tool that need to be designed should match this holder. Figure 4.29 shows the edge of the holder. As showed in figure4.30 and figure4.26, the size of notch A in figure4.30 should match the edge of holder so that

Figure 4.28: Top view of the holder of CHA Solution STD

4

Figure 4.29: The edge of the holder where wafer can be fixed on it and an original clamp of holder.

the tool for tilting can be clipped to the edge. Then, one side of wafer was inserted into one of three notches(B,C,D), and another side of wafer put on the edge of holder. After this step, clamp, as shown in figure4.29, was used to fix the wafer on the edge of holder.

Figure4.30 shows the tool that was designed for tilting the angle of the wafer when doing evaporation. 3 gears can be chosen with degree of $B = 3^0$, $C = 5^0$ and $D = 7^0$. This figure demonstrates how the tool works when doing the evaporation. By this tool, sidewall of pillars can be covered with metal. The distance between metal source of CHA solution STD and the wafer (dm) is quite long when it is compared to the structure size of pillars (um), therefore, the ejection of metal ions can be assumed to be parallel lines.

The thickness that can be covered on sidewall can be derived from Fig.4.31:

$$T_s = T * sin\beta \tag{4.14}$$

This T_s need to be as thicker as possible because tilting angle were very small (less then 10 degree) due to ensure all parts of pillars can be covered by metal. Maximum tilting angle will be discussed later. Equation 4.14 shows the thick of metal that on the sidewall is proportional to the tilting angle.
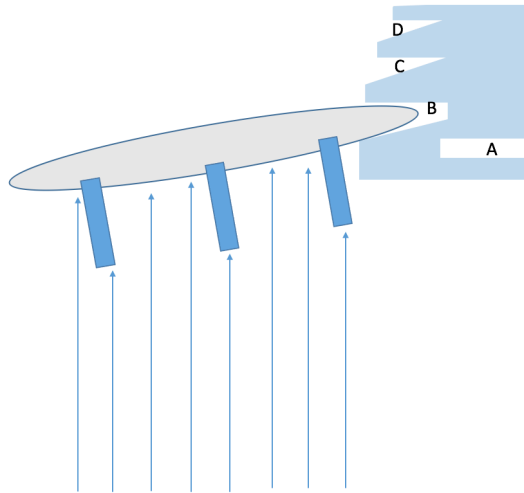
Figure 4.30: Clamp that help to do 4 time evaporation

a	h	a/h	β (radian)	β (in degree)
2,06	10	0,202	0,199317895	11,42007417
2,06	20	0,101	0,100658653	5,767315997
2,06	30	0,067333333	0,067231851	3,852101318
2,06	40	0,0505	0,050457136	2,89098096

Table 4.4: Table of relationship between pillar height and maximum tilting angle

At the same time, this angle should not larger than a certain value. As shown in Fig.4.32, if the angle larger than a degree, same part of the sidewall near the bottom of the pillars which is indicated in the red region will not be covered. This degree be derived from figure below:

$$\beta = \tanh \frac{a}{h} \qquad (4.15)$$

$$\frac{a}{h} = \tan \beta \qquad (4.16)$$

Equation4.16 shows, the limitation of the tilting angle is depend on the minimum distance between two pillars and the pillar height. The higher pillars or the smaller distance between will both limit the maximum tilting angle.

Figure 4.34 shows that the minimum distance between two pillar is 2.06um. Table4.4 below list the maximum tilting angle depending on the height of pillar.

In previous chapter, minimum thickness of platinum have been calcu-
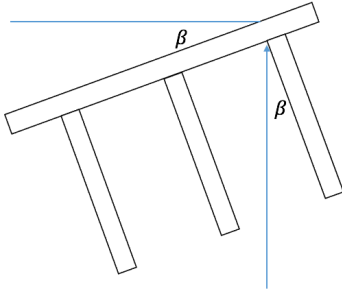
Figure 4.31: Calculation of thickness of metal that can be deposited on the sidewall of pillars.
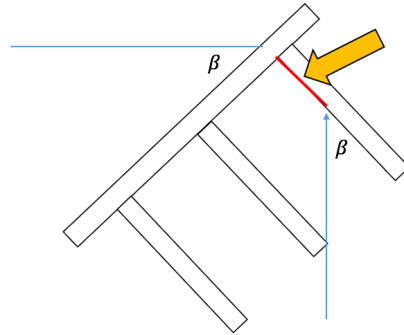
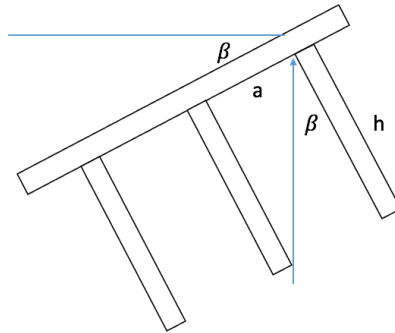Figure 4.32: The largest angle that the wafer can be tilted

4

Figure 4.33: Calculation of maximum tilting angle

lated which is 5.94nm. Therefore:

$$T_s = T * sin\beta > 5.94nm \tag{4.17}$$

At the same time, the total amount of platinum should be controlled because platinum is expensive. Assume the amount of platinum of one time evaporation should not exceed 200nm, than the minimum tilting angle is:

$$\beta > \sinh \frac{T_s}{T} = \sinh \frac{5.94nm}{200nm} = 1.7^o \tag{4.18}$$

Then the tilting angle of the tool can be decided depending on how height the pillars need to be evaporated. For example, if 20um height pillars need to be evaporated, than then maximum tilting degree is 5.77^o as showed in Table 4.4 and the minimum tilting angle is 1.7^o.
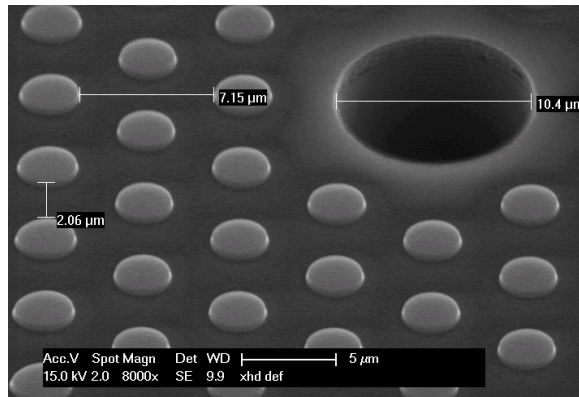
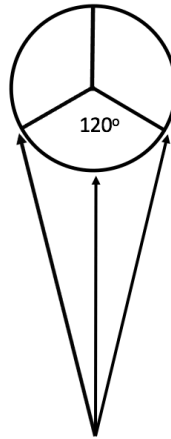Figure 4.34: Distances between two pillar

Four times evaporation

Figure 4.35: The maximum coverage that one time evaporation can achieve

As the figure 4.35 shows, only part of the sidewall of pillars can be covered by metal with one time evaporation. In order to cover everywhere of pillars, at least four times of evaporation should be done. Among them, three times of evaporation are need to be done under the help of tilting tool so that to ensure the total sidewall of pillars are covered by metal. Wafer should be rotated 120° for each time of evaporation, therefore, the evaporation can cover 360° for whole circle. The fourth time of evaporation is done for bottom of structure.

As figure 4.36 shows, if the wafer is deposited under the condition of maximum tilting angle, the pillar will block the ions of metal to reach the bottom of wafer. As the region showed in figure 4.36, this bottom plane will
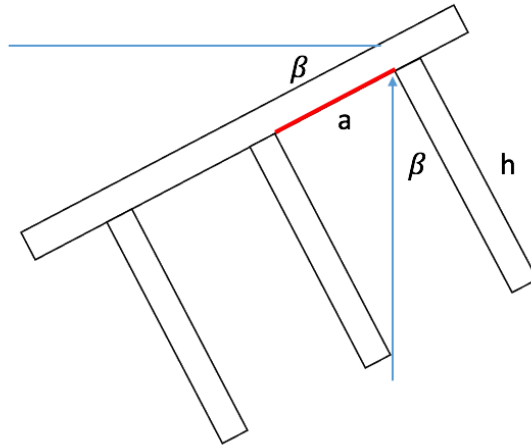
Figure 4.36: Evaporation under maximum tilting angle.

not be covered by metal. Thus, another time of evaporation without tilting tool is necessary to make sure the whole structure are covered by metal.

4.2.5. Measurement Result of Flowchart two

Processing was successful for both Pt. whole sensor structure can be got by the process and Four-Times-Evaporation were also success to address the problem of evaporation on sidewall of pillar. The measurement results were shown below.
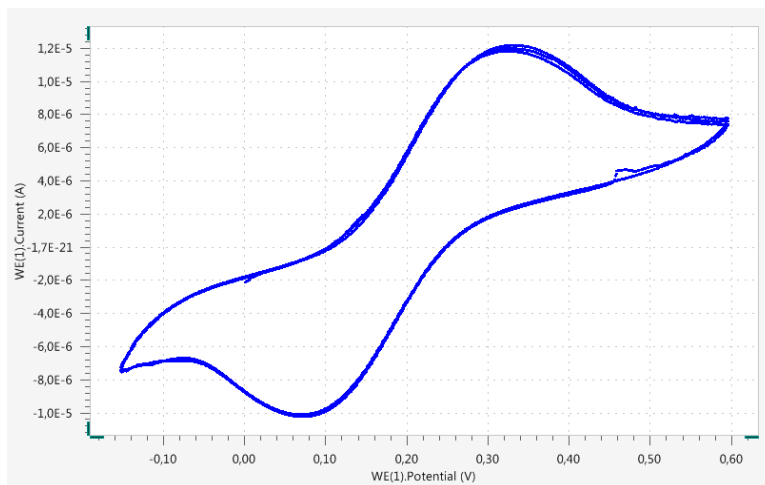

Figure 4.37: Cyclic Voltammatric measurement of plain sample without pillars.

As can be seem from the figure4.37, current peak of oxidation and reduction were very clear at the voltage 3.5V and 0.8V respectively which indicated that there were redox reaction in the solution when Pt was used as working electrode. However, after around 15 minutes, the measurement result became to change. Finally, the measurement result changed to the result as figure4.38 showed below.

As figure4.38 indicates, current increased dramatically to around 30uA and the redox behavior disappeared. And it showed the ohm behavior with which the current were proportional to voltage. And for all samples including samples with pillars had same problem. In the first 5 minutes after packaging of sample, the measurement result showed good result. However, if the sample was tested after 20 minutes, the current would increase and there was no redox behavior anymore.

Same problem occurred that after few minutes measurement the output result became no redox behavior and current increased drastically. The figure4.39 shows four runs of cycle measurement which means when one time measurement finished, the machine continued to do second run of measurement and draw I-V graph in the same graph. Graduation increasing of current could be seem and finally the result became the one shown in figure4.40. The most likely reason for this phenomenon was the packaging method is not feasible or the packaging material was not suitable. Then different packaging materials were tested including non-conductive
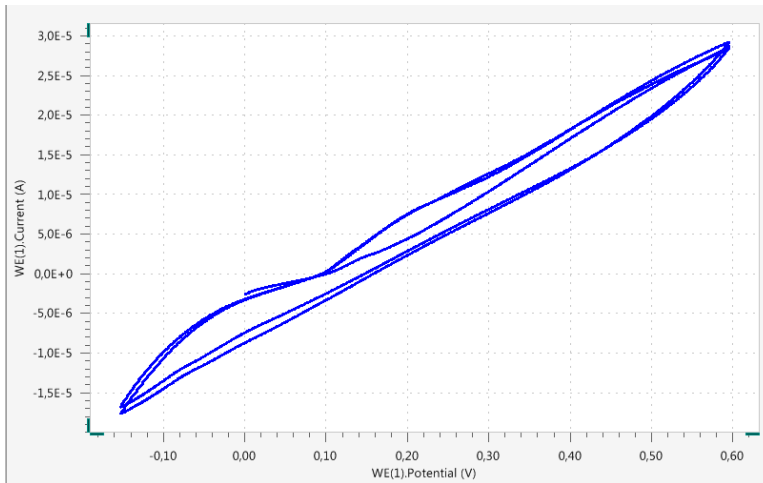
Figure 4.38: Cyclic Voltammatric measurement of plain sample without pillars
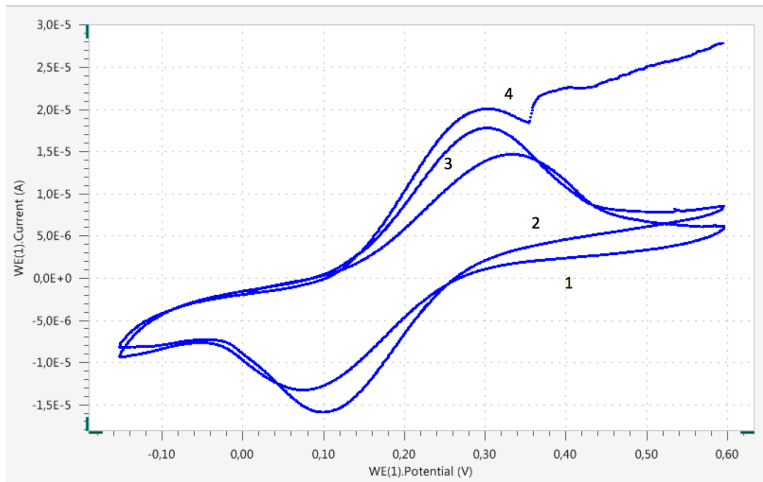

Figure 4.39: Cyclic Voltammatric measurement of sample with pillars

glue, PDMS and epoxy. However, all of these packaging material gave same results. The most likely reason is the packaging material can not block the testing solution($3 mM K3[Fe(CN)6] in 0.1 M KCl electrolyte solution$) so that the solution penetrated into the glue and react with other metal such as gold(wire) and silver(connector). The reason why packaging failed need further investigation.
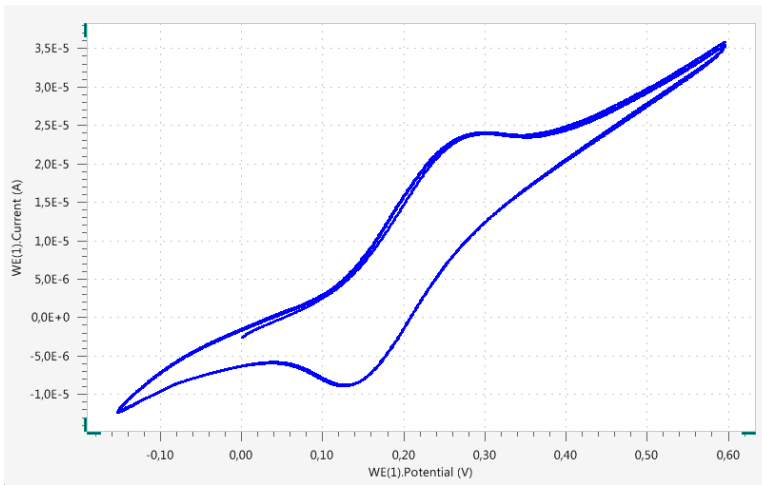
Figure 4.40: Cyclic Voltammatric measurement of sample with pillars

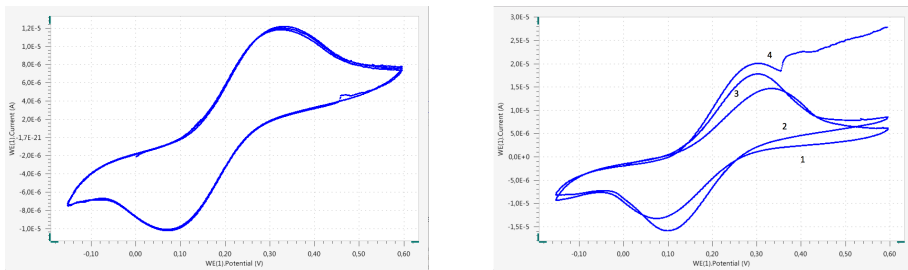## **4.3.** Challenge And Result of Flowchart Three

Figure 4.41: Comparison of plain samples and samples with pillars.

From the results of flowchart two, current of sample with pillars are larger than plain sample. The increased ratio was around:

$$r_i = \frac{20um}{12} \approx 1.667 \tag{4.19}$$

Although the current did increase, this increased aspect ratio was far from the aspect ratio 10.67 that was calculated in previous simulation part. One possible reason was that platinum did not cover the whole pillar structure. This means the actually surface area of electrode was less than the area value derived from calculation.

Figure4.42,4.43 and 4.44 were the SEM photos of pillars which were etched by the recipe "AJ_Mapper_Speed". Platinum had already covered the structure as figure4.42 show because the color was bright white on the top of pillars. When it was zoom in as figure4.43 and figure 4.44 shown,
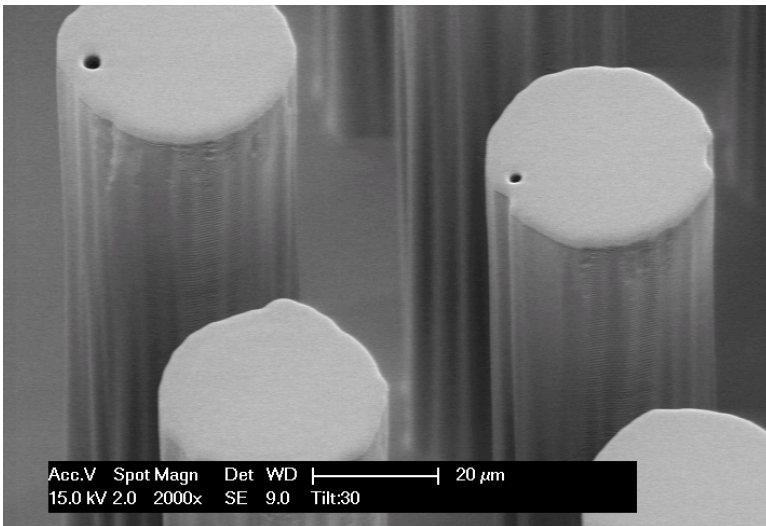
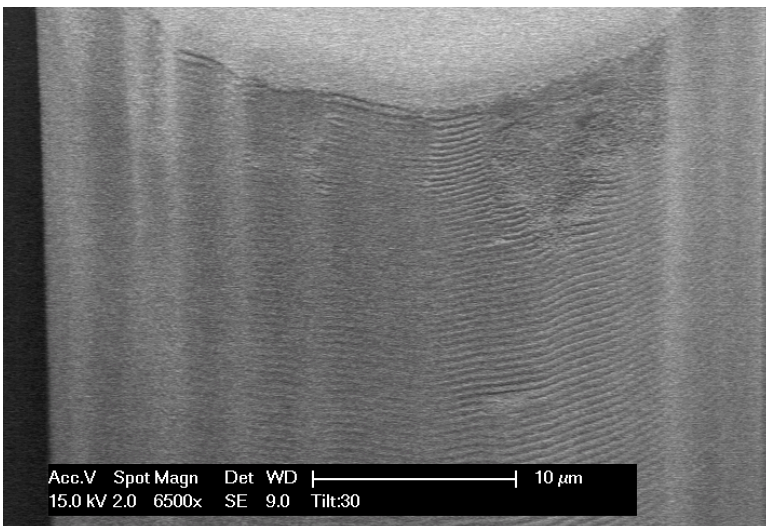Figure 4.42: SEM photo of pillars which were etched by the recipe "AJ_Mapper_Speed"

Figure 4.43: SEM photo of pillars which were etched by the recipe "AJ_Mapper_Speed"

scalloping could be seem. However, these photos still could not judge if the coverage was good or not. In order to check the coverage of platinum, BEC SEM was used.

From the BEC SEM photo 4.45, clear scallop could be seem and the surface of sidewall of pillars were not totally covered This was the reason why the aspect ratio of flowchart two was not as high as expect. From the
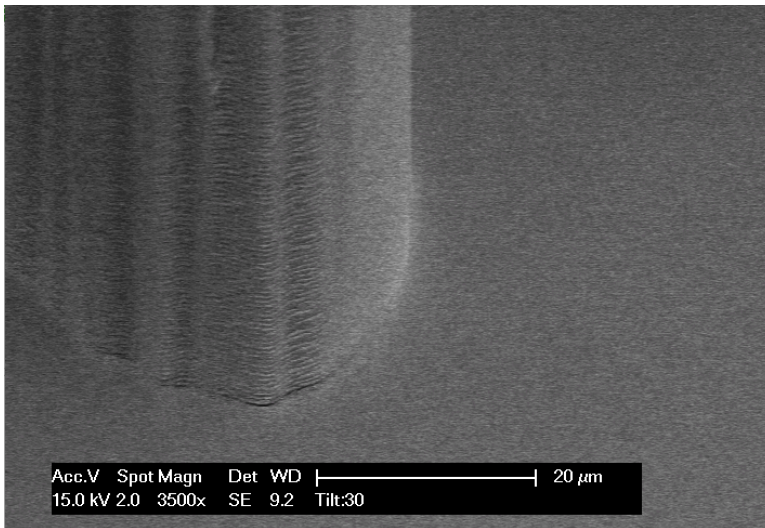
Figure 4.44: SEM photo of pillars which were etched by the recipe "AJ_Mapper_Speed"
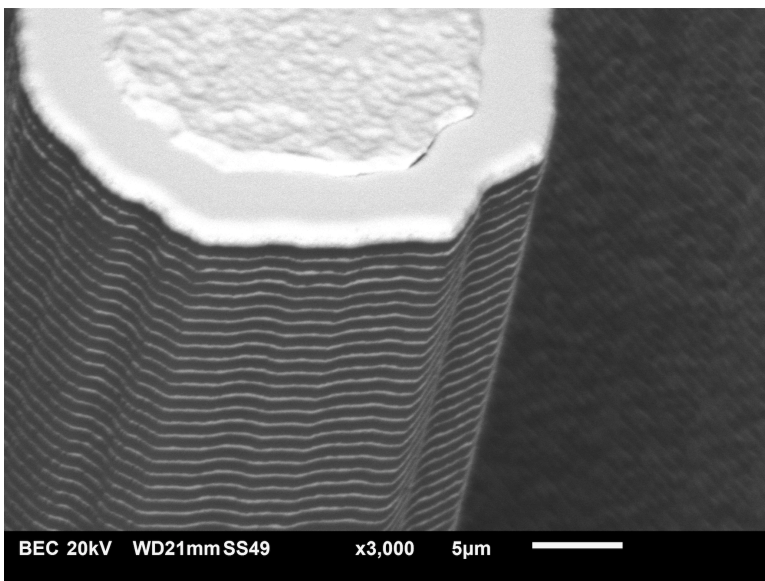

Figure 4.45: BEC SEM photo of pillars which were etched by the recipe "AJ_Mapper_Speed"

BEC SEM photo 4.46, bottom plain and top surface were already totally covered by platinum.
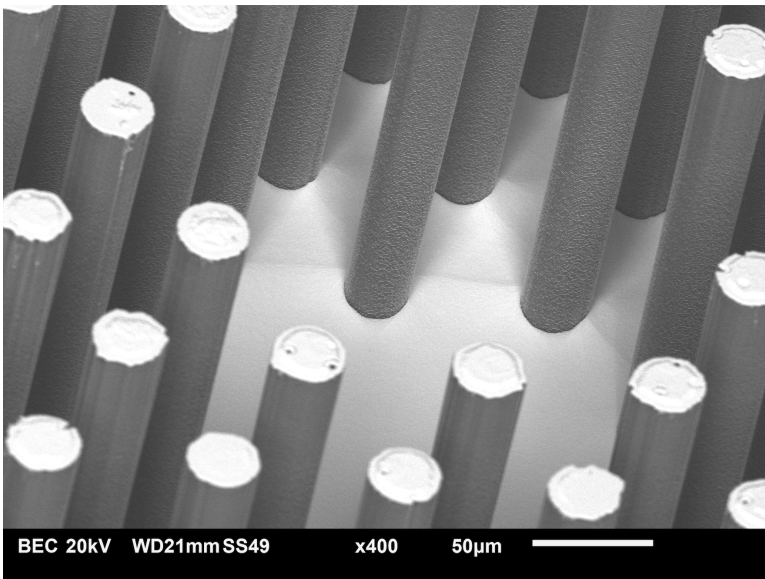
Figure 4.46: BEC SEM photo of pillars which were etched by the recipe "AJ_Mapper_Speed"

4.3.1. Increasing the Coverage of Platinum

In order to increase the coverage of platinum on the sidewall of pillars, making surface of pillars smooth was necessary. The efficient way to achieve it is changing the recipe of DRIE etching or using none Boson etch. Two methods had been tested and proved to be good.

Using Recipe"xxEKL-SmoothXXX" For DRIE Etching

Recipe"ekl-Smoothxxx" was used because this recipe could get smoother pillars than other recipe. Another important reason was the pillars etched by this recipe had positive profile angle as the figure 4.51 shown. The profile angle of pillars shown in figure4.51 was:

$$\beta = 90^o + \tanh \frac{\frac{32.5-30.3}{2}}{22.1um} = 92.85^o \tag{4.20}$$

The reason why positive profile angle was better than other profile angles can be seen from figure

As figure 4.48 shows, only region of pillars with 90^0 profile angle can be covered by platinum. The purple region can not be deposited by Pt because the edge of red region block the Pt ions. As figure 4.49 shows, if pillars have positive profile angle, the purple region can also be deposited as the region. Thus the positive profile angle is the better choice to improve the coverage of metal.

BEC SEM photo 4.51 shows, half of the surface area on low region of sidewall had already been smoothed. Scalloping still exist ed on another

Acc.V   Spot Magn   Det WD
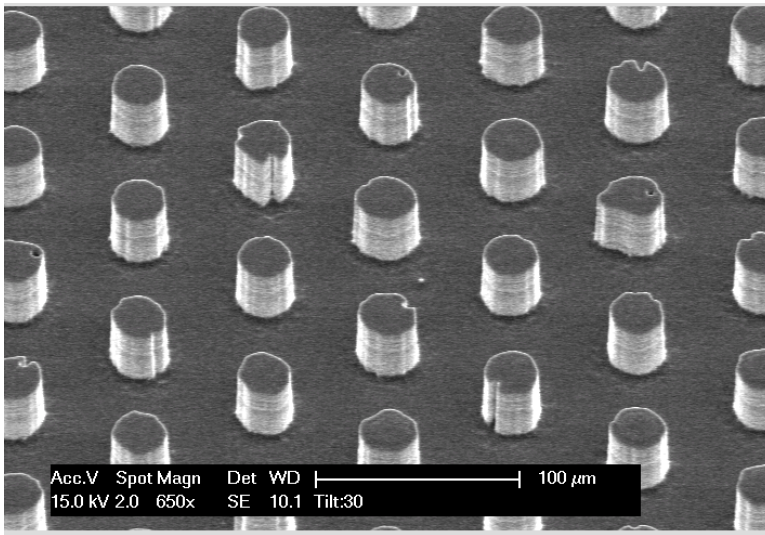15.0 kV 2.0   650x   SE   10.1 Tilt:30   100 μm

Figure 4.47: SEM photo of pillars which were etched by the recipe "xxEKL-Smoothxxx"
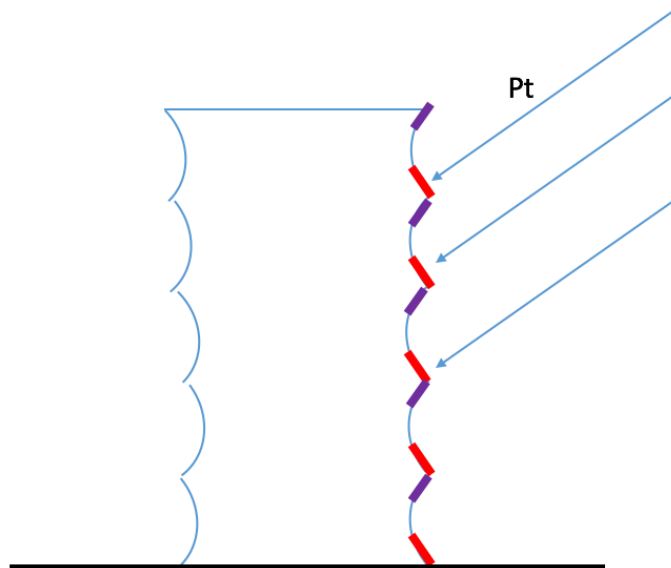

Figure 4.48: Coverage of metal when scalloping exist on the sidewall of pillars with 90° profile angle

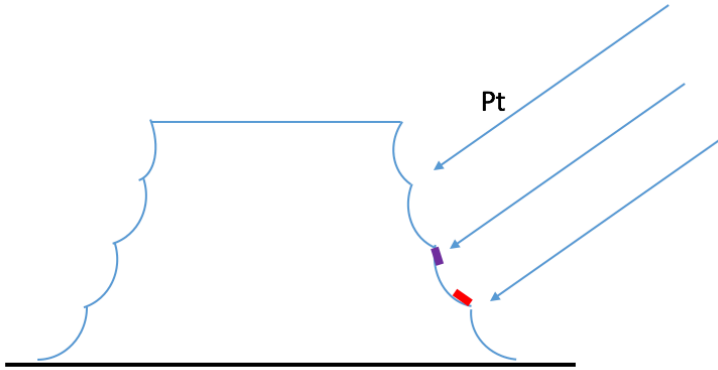half part on the up region of sidewall of pillars. This means the recipe

Figure 4.49: Coverage of metal when scalloping exist on the sidewall of pillars with positive profile angle
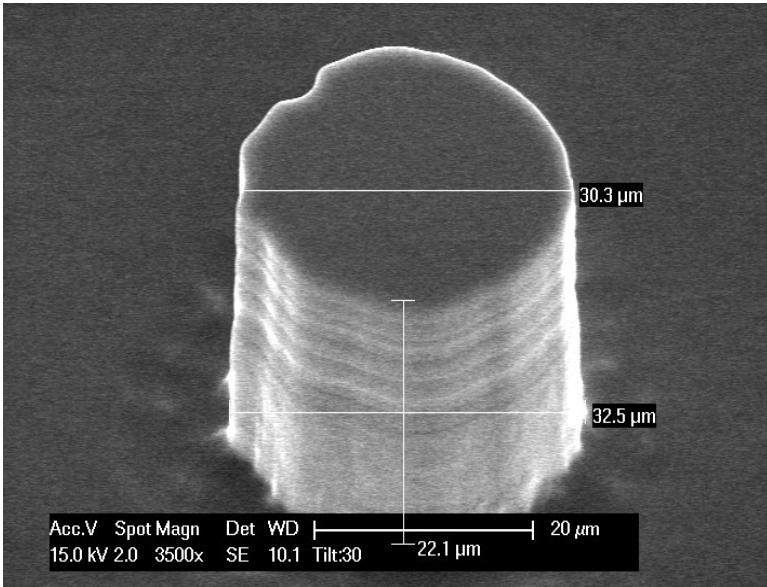

Figure 4.50: SEM photo of pillars which were etched by the recipe "xxEKL-Smoothxxx"

"xxEKL-Smoothxxx" could make the surface of pillars smooth but only for the low region of pillars. Therefore, making shorter pillars smooth was possible. The height of pillars of figure 4.51 was:

$$h = \frac{h_{SEM}}{cos\beta} = \frac{30.803}{\frac{\sqrt{2}}{2}} = 43.562 \tag{4.21}$$

Thus, the maximum height of pillars with smooth sidewall was half of
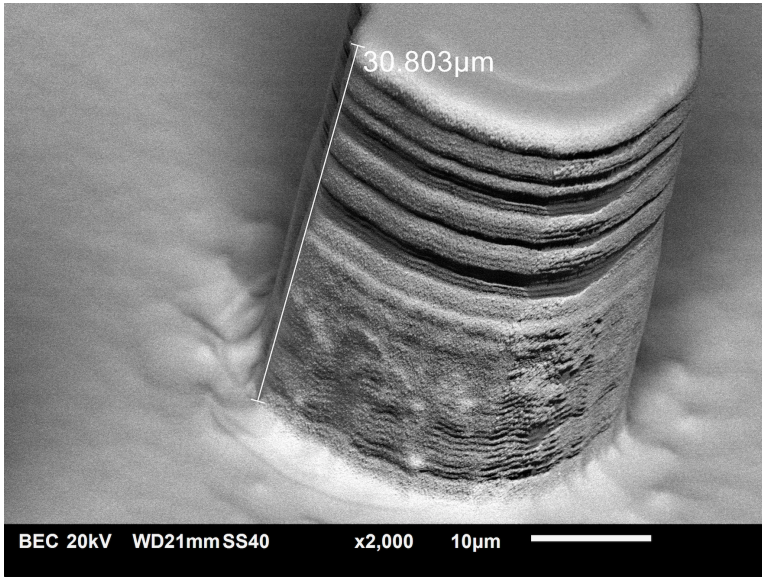
30.803µm

BEC 20kV WD21mm SS40   x2,000   10µm

Figure 4.51: BEC SEM photo of pillars which were etched by the recipe "xxEKL-Smoothxxx"

the height of the pillars showed in figure4.51

$$h_{max} = \frac{h}{2} = 21.78um \tag{4.22}$$

One possible reason was that power would increase when Rapier etched deep into si trench. Then the passivation layer was not strong enough anymore to protect the sidewall.

Non Boson Etching

The scalloping appeared duo to Boson etch. Thus, none Boson etching had been tried in "Trikon Omega 201" with recipe "Deep-Si".

As the figure 4.53 shows, recipe "deep-Si" of Trikon Omega 201 can also achieve nearly straight pillars. The profile angle was:

$$\beta = \tanh \frac{31.3um}{\frac{22.3um - 20um}{2}} \times \frac{180^o}{\pi} \approx 87.94^o \tag{4.23}$$

Although it was negative profile angle, there was no scalloping on the side wall and this angle would not effect the evaporation. From Previous section 4.2 , the maximum tilting angle was limited by distance of pillars and height of pillars. The distance between two pillars for file mask was around 43.63um as shown in figure 4.34

and the height of pillars is around:

$$h = 46.47um \times \sqrt{2} \approx 65.71um \tag{4.24}$$
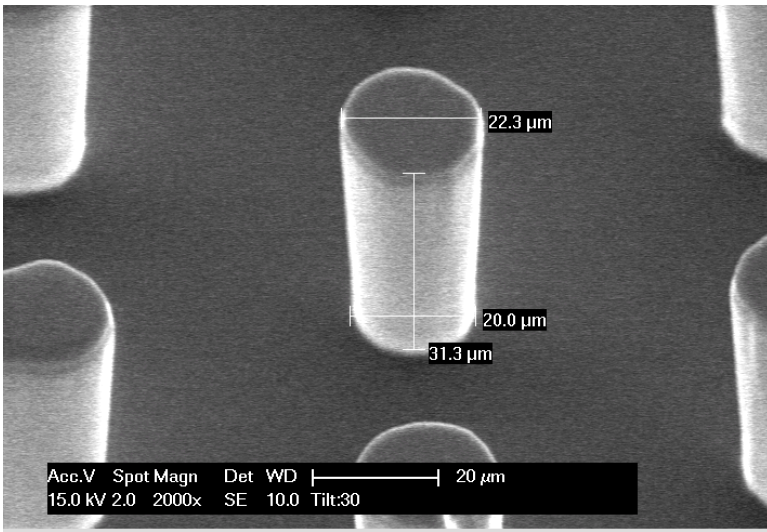
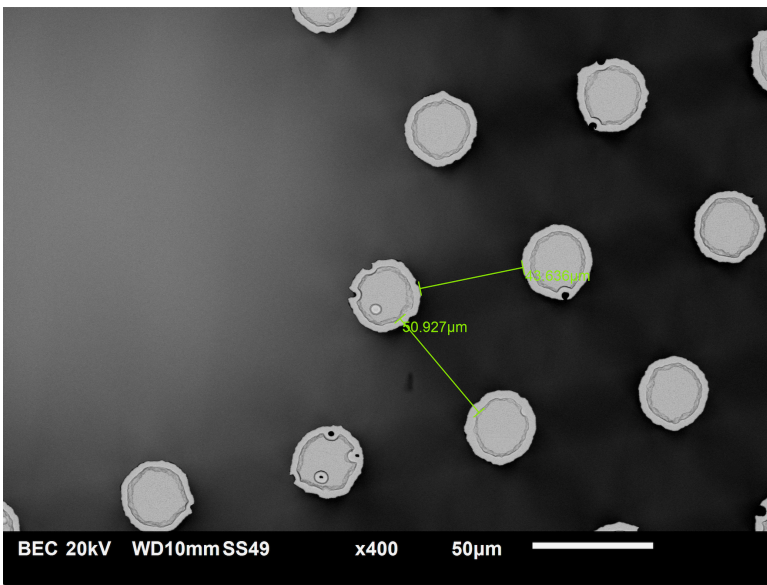Figure 4.52: SEM photo of pillars which were etched by the recipe "Deep-Si" in "Trikon Omega 201"

Figure 4.53: Scales of pillars and distance between two pillars of file mask

Where $\sqrt{2}$ means the tilting angle of BEC SEM inspection was 45°. From equation4.15, maximum tilting angle was:

$$\beta = \tanh \frac{a}{h} = \tanh \frac{43.63um}{65.71um} \approx 33.58^o \qquad (4.25)$$

Therefore, there was no problem to do evaporation with tilting tool. Because the tilting degree could be $3^o, 5^o$ and 7° for the tilting tool. All of these degree were within the range $1.18^o < \beta < 33.58^o$ This means no sidewall of pillars were blocked by other pillars when they were evaporated by platinum when tilting tool was used. If 7° tilting was used, the thick of platinum on sidewall was:

$$t_s = T * sin\beta = 200nm \times sin7^o \approx 24.37nm \tag{4.26}$$

If new tilting tool for file mask could be made, the maximum thickness platinum of sidewall of pillars could be :

$$t_{max} = T * sin\beta = 200nm * sin33.58^o \approx 110.62nm. \tag{4.27}$$
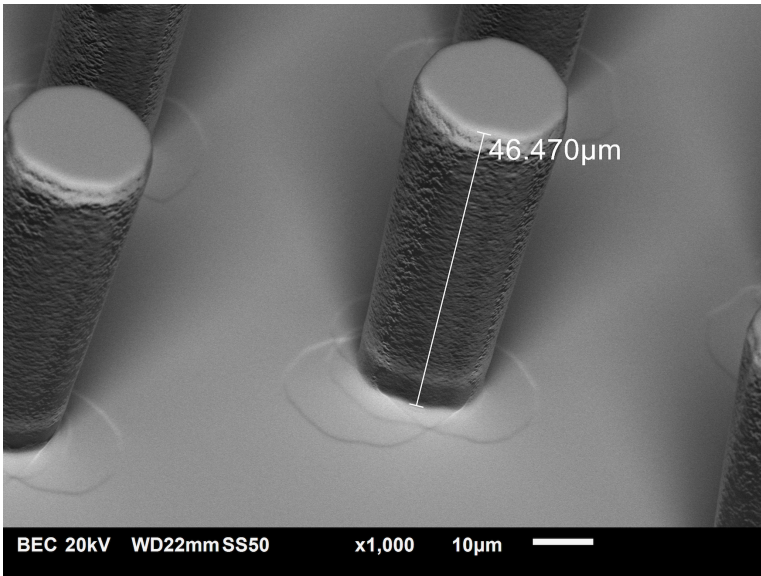

Figure 4.54: BEC SEM photo of pillars which were etched by the recipe "Deep-Si" in "Trikon Omega 201"

Figure 4.54 shows BEC SEM of pillars that etched by "recipe deep" of "Trikon Omega 201". From this photo, 3 times evaporation by using tilting tool were proved to be successful because there were three circles near bottom of pillars and these three circles covered total 360° of around pillars. There was no scalloping anymore.

From figure4.55, A and B parts had good uniform color with the bottom and had clear edges. This indicated that sidewall of A and B parts had already covered by platinum and the thickness of these two regions were thicker than the region c between them. That was why the region between A and B part showed darker color. The differences of thickness among A, B and C can be explained by the figure below.
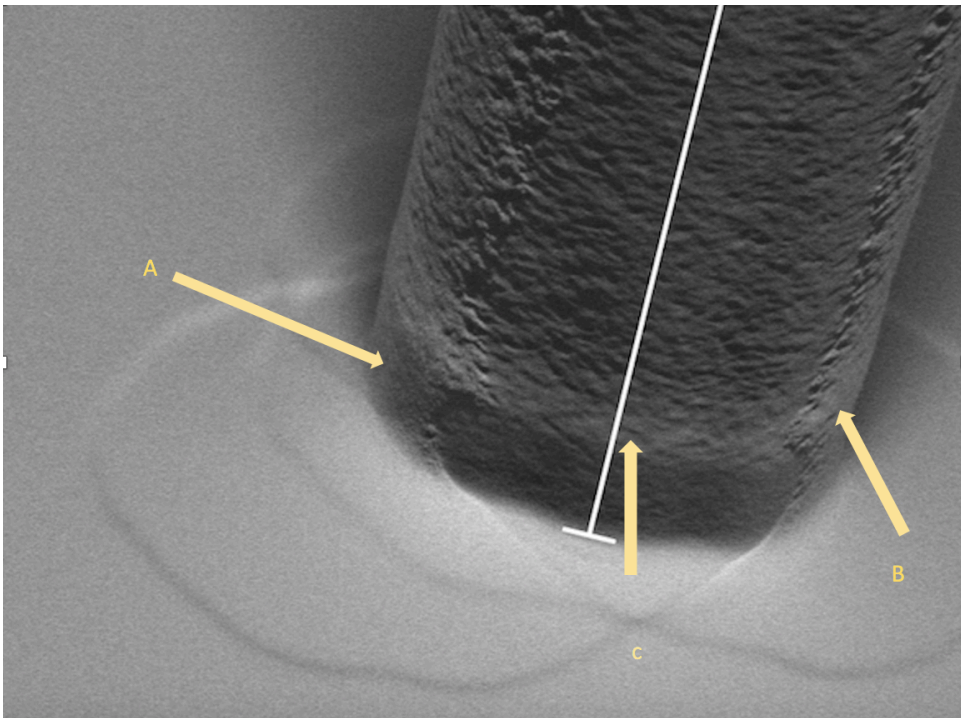
Figure 4.55: BEC SEM photo of pillars which were etched by the recipe "Deep-Si" in "Trikon Omega 201"

As figure 4.56 shows, vector $\vec{T}$ could be separated to two component vector $\vec{m}$ and $\vec{n}$. the thickness of platinum on point C was:

$$|\overline{m}| = |\vec{T}| \times cos\alpha = 200nm \times cos60^o = 100nm \qquad (4.28)$$

Because the thickness of A and B region were thicker than C region, different colors could be seem in SEM.

4

Figure 4.56: Calculation of the thickness of the platinum along the circle edge

5

Conclusion and Future Work

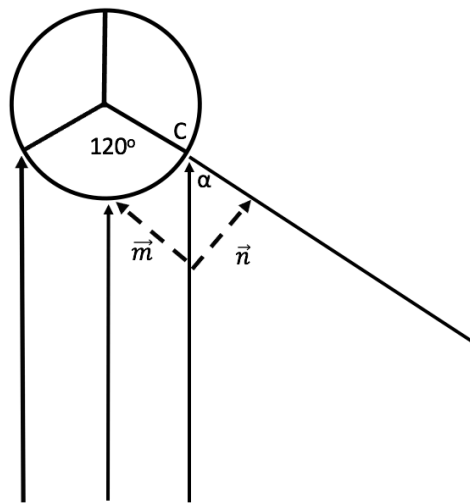In this work the design, the simulation and the fabrication of high aspect ratio electrochemical sensor has been done. The main goal of this thesis work is to design a 3D high aspect ratio electrochemical sensor base on MEMS technology. During this work, various challenges have been presented ranging from designing to processing.

5.1. Conclusion

* For Simulation, comsol model were built to calculate the aspect ratio and minimum thickness of platinum. It shows huge computation for the 3D model of the this electrochemical sensor both for the calculation of aspect ratio and the minimum thickness of platinum. Thus, equivalent 2D model was built and the formula has been derived for both model.

* For process one , by trying different recipe, pillar structures with profile angle 90 was got. The challenge for process one is time control of wet etching and the protection of pillars in front side. Wafer is easy to be etched through and pillar structures are destroyed. As mentioned in previous chapter, some TMAH will penetrate TEOS protection layer and destroy wafer.

* As for process two, two materials have been tested as working electrode TiN and Pt. TiN is shown to be not suitable material for working electrode of electrochemical sensor. There was no redox reaction when it was used as working electrode in electrochemical solution. The challenge came from the evaporation of platinum. Novel tilting tool has been designed by which deposition of pt for 3D structure in Evaporator became possible. However, measurement result showed

unstable result due to proper packaging method. The solution penetrate into PDMS and react with other material such as gold wire and silver connect. Further more, the current did not reach as high as theoretical value. only 2 times large than plain electrode. This was because there was scalloping on the sidewall of pillars.

* In third process, wire and connect were designed in wafer level. All of these were evaporated by platinum to ensure there was no other signal except Pt. Process three address the problem of scalloping by using recipe "xxeklsmoothxxx" of Rapier and by using no Boson etching recipe "deep-Si"in Omega. The disadvantage of xxeklsmoothxxx was that it can not etch very deep to get high pillar. Only pillars below 20um will have smooth sidewall surface. The disadvantage of non-Boson etching is that it do not suitable for small structure. If the distance of two pillars less than 30um, pillar will fall due to no passivation layer.

5.2. Future Work

There is still no perfect recipe to get pillars without scalloping. Even through, pillar structure without scalloping can be got by using "Trikon Omega 201", this recipe can not be used to etch small structure. The pillars with smooth sidewall achieved by recipe "EKL-smooth" but only 20um. Future work should focus on improve the recipe of DREI etching to smooth the higher pillar or find ways to use "Trikon Omega 201" to etch smaller structure. Feasible packaging method should be found to get more reliable measurement.

References

[1] N. R. Stradiotto, H. Yamanaka, and M. V. B. Zanoni, *Electrochemical sensors: a powerful tool in analytical chemistry,* Journal of the Brazilian Chemical Society **14**, 159 (2003).

[2] C. M. Brett and A. M. Oliveira-Brett, *Electrochemical sensing in solution—origins, applications and future perspectives,* Journal of Solid State Electrochemistry **15**, 1487 (2011).

[3] G. C. Barker and I. L. Jenkins, *Square-wave polarography,* Analyst **77**, 685 (1952).

[4] C. M. Brett and A. M. Oliveira-Brett, *Electrochemical sensing in solution—origins, applications and future perspectives,* Journal of Solid State Electrochemistry **15**, 1487 (2011).

[5] S. Zuo, Y. Teng, H. Yuan, and M. Lan, *Direct electrochemistry of glucose oxidase on screen-printed electrodes through one-step enzyme immobilization process with silica sol–gel/polyvinyl alcohol hybrid film,* Sensors and actuators B: Chemical **133**, 555 (2008).

[6] E. V. Mosharov and D. Sulzer, *Analysis of exocytotic events recorded by amperometry,* Nature methods **2**, 651 (2005).

[7] J. L. Peters, L. H. Miner, A. C. Michael, and S. R. Sesack, *Ultrastructure at carbon fiber microelectrode implantation sites after acute voltammetric measurements in the striatum of anesthetized rats,* Journal of neuroscience methods **137**, 9 (2004).

[8] C. Schabmueller, D. Loppow, G. Piechotta, B. Schütze, J. Albers, and R. Hintsche, *Micromachined sensor for lactate monitoring in saliva,* Biosensors and Bioelectronics **21**, 1770 (2006).

[9] A. Ayon, K.-S. Chen, K. Lohner, S. Spearing, H. Sawin, and M. Schmidt, *Deep reactive ion etching of silicon,* in *MRS Proceedings*, Vol. 546 (Cambridge Univ Press, 1998) p. 51.

[10] J. Laconte, D. Flandre, and J. P. Raskin, *Silicon bulk micromachining with tmah,* Micromachined Thin-Film Sensors for SOI-CMOS Co-Integration , 17 (2006).

[11] K. Miller, M. Li, K. M. Walsh, and X.-A. Fu, *The effects of drie operational parameters on vertically aligned micropillar arrays,* Journal of Micromechanics and Microengineering **23**, 035039 (2013).

[12] C. Zhu, G. Yang, H. Li, D. Du, and Y. Lin, *Electrochemical sensors and biosensors based on nanomaterials and nanostructures,* Analytical chemistry **87**, 230 (2014).

5

6

ACKNOWLEDGEMENTS

First I would like to thank Prof Kouchi for giving me the opportunity to do my thesis under his supervision and guidance. The past year has proved to be an exciting year where I learned not only how to design a sensor but also how to fabricate it. Even though, there are so many challenge and difficult, I learned much knowledge and got experience for clean room work. On this journey I met many challenges and with the knowhow provided in this group and by the EKL lab engineers a success story was born. For the most part I would like to thank dr. Jia Wei and PhD. Manjunath Ramachandrappa Venkatesh for all their guidance and patience. Then I would like to thank My parents who gave me the expensive tuition fee. I would like to thank the people working in the EKL lab, dr. Henk van Zeijl and all the engineers who provided their insightful knowledge in the processing. Lastly I would like to thank all the people at the EKL who are wonderful people and have shown patience. Also I would like to thank my girlfriend HongZhang who support me when I met difficulty and was in low mood.